A&A 562, A53 (2014)
DOI: 10.1051/0004-6361/201322681
© ESO 2014

Astronomy & Astrophysics

Mean-field and direct numerical simulations of magnetic flux concentrations from vertical field

A. Brandenburg[1,2], O. Gressel[1,3], S. Jabbari[1,2], N. Kleeorin[4,1,5], and I. Rogachevskii[4,1,5]

[1] Nordita, KTH Royal Institute of Technology and Stockholm University, Roslagstullsbacken 23, 10691 Stockholm, Sweden
e-mail: brandenb@nordita.org
[2] Department of Astronomy, AlbaNova University Center, Stockholm University, 10691 Stockholm, Sweden
[3] Niels Bohr International Academy, Niels Bohr Institute, Blegdamsvej 17, 2100 Copenhagen Ø, Denmark
[4] Department of Mechanical Engineering, Ben-Gurion University of the Negev, POB 653, 84105 Beer-Sheva, Israel
[5] Department of Radio Physics, N. I. Lobachevsky State University of Nizhny Novgorod, Russia

Received 16 September 2013 / Accepted 4 December 2013

ABSTRACT

Context. Strongly stratified hydromagnetic turbulence has previously been found to produce magnetic flux concentrations if the domain is large enough compared with the size of turbulent eddies. Mean-field simulations (MFS) using parameterizations of the Reynolds and Maxwell stresses show a large-scale negative effective magnetic pressure instability and have been able to reproduce many aspects of direct numerical simulations (DNS) regarding growth rate, shape of the resulting magnetic structures, and their height as a function of magnetic field strength. Unlike the case of an imposed horizontal field, for a vertical one, magnetic flux concentrations of equipartition strength with the turbulence can be reached, resulting in magnetic spots that are reminiscent of sunspots.
Aims. We determine under what conditions magnetic flux concentrations with vertical field occur and what their internal structure is.
Methods. We use a combination of MFS, DNS, and implicit large-eddy simulations (ILES) to characterize the resulting magnetic flux concentrations in forced isothermal turbulence with an imposed vertical magnetic field.
Results. Using DNS, we confirm earlier results that in the kinematic stage of the large-scale instability the horizontal wavelength of structures is about 10 times the density scale height. At later times, even larger structures are being produced in a fashion similar to inverse spectral transfer in helically driven turbulence. Using ILES, we find that magnetic flux concentrations occur for Mach numbers between 0.1 and 0.7. They occur also for weaker stratification and larger turbulent eddies if the domain is wide enough. Using MFS, the size and aspect ratio of magnetic structures are determined as functions of two input parameters characterizing the parameterization of the effective magnetic pressure. DNS, ILES, and MFS show magnetic flux tubes with mean-field energies comparable to the turbulent kinetic energy. These tubes can reach a length of about eight density scale heights. Despite being $\lesssim$1% equipartition strength, it is important that their lower part is included within the computational domain to achieve the full strength of the instability.
Conclusions. The resulting vertical magnetic flux tubes are being confined by downflows along the tubes and corresponding inflow from the sides, which keep the field concentrated. Application to sunspots remains a viable possibility.

Key words. sunspots – Sun: magnetic fields – turbulence – magnetic fields – hydrodynamics

1. Introduction

Sunspots and active regions are generally thought to be the result of magnetic fields emerging from deep at the bottom of the solar convection zone (Fan 2009). Alternatively, solar magnetic activity may be a shallow phenomenon (Brandenburg 2005). Several recent simulations with realistic physics of solar turbulent convection with radiative transfer have demonstrated the appearance of magnetic flux concentrations either spontaneously (Kitiashvili et al. 2010; Stein & Nordlund 2012) or as a result of suitable initial conditions (Cheung et al. 2010; Rempel 2011). There is also the phenomenon of magnetic flux expulsion, which has been invoked as an explanation of the segregation of magneto-convection into magnetized, non-convecting regions and non-magnetized, convecting ones (Tao et al. 1998).

The magneto-hydrothermal structure of sunspots has been studied using the thin flux tube approximation (Spruit 1981), in which the stability and buoyant rise of magnetic fields in the solar convection zone has been investigated. This theory has been also applied to vertical magnetic flux tubes, which open up toward the surface. An important property of such tubes is the possibility of thermal collapse, caused by an instability that leads to a downward shift of gas and a more compressed magnetic field structure; see Spruit (1979), who adopted a realistic equation of state including hydrogen ionization. On the other hand, sunspot simulations of Rempel (2011) and others must make an ad hoc assumption about converging flows outside the tube to prevent it from disintegrating due to turbulent convection. This approach also does not capture the generation process, that is now implicitly seen to operate in some of the simulations of Kitiashvili et al. (2010) and Stein & Nordlund (2012).

To understand the universal physical mechanism of magnetic flux concentrations, which has been argued to be a minimal model of magnetic spot formation in the presence of a vertical magnetic field (Brandenburg et al. 2013), we consider here forced turbulence in a strongly stratified isothermal layer without radiation. In the past few years, there has been significant progress in modelling the physics of the resulting magnetic flux concentrations in strongly stratified turbulence via the negative effective magnetic pressure instability (NEMPI). The

physics behind this mechanism is the suppression of total (hydrodynamic plus magnetic) turbulent pressure by a large-scale magnetic field. At large enough magnetic Reynolds numbers, well above unity, the suppression of the total turbulent pressure can be large, leading to a negative net effect. In particular, the effective magnetic pressure (the sum of non-turbulent and turbulent contributions) becomes negative, so that the large-scale negative effective magnetic pressure instability is excited (Kleeorin et al. 1989, 1990, 1993, 1996; Kleeorin & Rogachevskii 1994; Rogachevskii & Kleeorin 2007).

Hydromagnetic turbulence has been studied for decades (Biskamp 1993), but the effects of a large-scale magnetic field on the total pressure are usually ignored, because in the incompressible case the pressure can be eliminated from the problem. This changes when there is gravitational density stratification, even in the limit of small Mach number, because $\boldsymbol{\nabla}\cdot\rho\boldsymbol{U}=0$ implies that $\boldsymbol{\nabla}\cdot\boldsymbol{U}=U_z/H_\rho\neq 0$. Here, $\boldsymbol{U}$ is the velocity, $H_\rho=|\mathrm{d}\ln\rho/\mathrm{d}z|^{-1}$ is the density scale height, and gravity points in the negative z direction. When domain size and gravitational stratification are big enough, the system can become unstable with respect to NEMPI, which leads to a spontaneous accumulation of magnetic flux. Direct numerical simulations (DNS) with large scale separation have been used to verify this mechanism for horizontal magnetic fields (Brandenburg et al. 2011; Kemel et al. 2012a, 2013). In that case significant progress has been made in establishing the connection between DNS and related mean-field simulations (MFS). Both approaches show that the resulting magnetic flux concentrations are advected downward in the nonlinear stage of NEMPI. This is because the effective magnetic pressure is negative, so when the magnetic field increases inside a horizontal flux structure, gas pressure and density are locally increased to achieve pressure equilibrium, thus making the effective magnetic buoyancy force negative. This results in a downward flow ("potato-sack" effect). Horizontal mean magnetic fields are advected downward by this flow and never reach much more than a few percent of the equipartition field strength.

The situation is entirely different for vertical magnetic fields. The downflow draws gas downward along magnetic field lines, creating an underpressure in the upper parts, which concentrates the magnetic field to equipartition field strength with respect to the turbulent kinetic energy density (Brandenburg et al. 2013). The resulting magnetic flux concentrations have superficially the appearance of sunspots. For horizontal fields, spots can also form and they have the appearance of bipolar regions, as has been found in simulations with a coronal layer above a turbulent region (Warnecke et al. 2013). However, to address the exciting possibility of explaining the occurrence of sunspots by this mechanism, we need to know more about the operation of NEMPI with a vertical magnetic field. In particular, we need to understand how it is possible to obtain magnetic field strengths much larger than the optimal magnetic field strength at which NEMPI is excited. We will do this through a detailed examination of magnetic flux concentrations in MFS, where the origin of flows can be determined unambiguously owing to the absence of the much stronger turbulent convective motions.

We complement our studies with DNS and so-called "implicit large-eddy" simulations (ILES), which are comparable to DNS in that they aim to resolve the inertial range of the forced turbulence. ILES differ from DNS in that one does not attempt to resolve the dissipation scale, which is numerically expensive due to resolution requirements. In short, ILES are DNS without explicit physical dissipation coefficients. However, unlike large-eddy simulations, no turbulence parameterization model is used at all to represent the unresolved scales. Lacking explicit dissipation, ILES instead rely on suitable properties of the truncation error of the numerical scheme (Grinstein et al. 2005), which guarantees that kinetic and magnetic energies are dissipated near the grid scale. In the finite-volume code Nirvana (Ziegler 2004) that we use for ILES here, dissipation occurs in the averaging step of the Godunov scheme. The advantage of the finite-volume scheme is the ability to capture shocks without explicit or artificial viscosity. This allows us to probe the regime of higher Mach numbers without the requirement to adjust the Reynolds number or grid resolution.

Following earlier work of Brandenburg et al. (2011), we will stick to the simple setup of an isothermal layer. This is not only a computational convenience, but it is also conceptually significant, because it allows us to disentangle competing explanations for sunspot and active region formation. One of them is the idea that active regions are being formed and held in place by the more deeply rooted supergranulation network at 20–40 Mm depth (Stein & Nordlund 2012). In a realistic simulation there will be supergranulation and large-scale downdrafts, but NEMPI also produces large-scale downdrafts in the nonlinear stage of the evolution. However, by using forced turbulence simulations in an isothermal layer, an explanation in terms of supergranulation would not apply.

We emphasize that an isothermal layer can be infinitely extended. Furthermore, the stratification is uniform in the sense that the density scale height is independent of height. Nevertheless, the density varies, so the equipartition magnetic field strength also varies. Therefore, the ratio of the imposed magnetic field strength to the equipartition value varies with height. NEMPI is excited at the height where this ratio is around 3% (Losada et al. 2013). This explains why NEMPI can be arranged to work at any field strength if only the domain is tall enough.

At large domain size, DNS and ILES become expensive and corresponding MFS are an ideal tool to address questions concerning the global shape of magnetic flux concentrations. In that case, significant conceptual simplifications can be achieved by making use of the axisymmetry of the resulting magnetic flux concentrations. We also need to know more about the operation of NEMPI under conditions closer to reality. For example, how does it operate in the presence of larger gravity, larger Mach numbers, and smaller scale separation? This aspect is best being addressed through ILES, where significant dissipation only occurs in shocks.

We consider three-dimensional (3D) domains and compare in some cases with MFS in two-dimensions (2D) using axisymmetry or Cartesian geometry. Here, axisymmetry is adequate for vertical tubes while Cartesian geometry is adequate for vertical sheets of horizontal magnetic field. The MFS provide guidance that is useful for understanding the results of DNS and ILES, so in this paper we begin with MFS, discuss the mechanism of NEMPI and then focus on the dependencies on gravity, scale separation, and Mach numbers using DNS. Finally, we assess the applicability of NEMPI to sunspot formation.

2. Mean-field study of NEMPI

For the analytical study of NEMPI with a vertical field we consider the equations of mean-field MHD for mean magnetic field $\overline{\boldsymbol{B}}$, mean velocity $\overline{\boldsymbol{U}}$, and mean density $\overline{\rho}$ in the anelastic approximation for low Mach numbers, and for large fluid and

magnetic Reynolds numbers,

$$\frac{\partial \overline{\boldsymbol{B}}}{\partial t} = \boldsymbol{\nabla} \times \left(\overline{\boldsymbol{U}} \times \overline{\boldsymbol{B}} - \eta_{\rm t} \mu_0 \overline{\boldsymbol{J}} \right), \tag{1}$$

$$\overline{\rho} \frac{{\rm D}\overline{\boldsymbol{U}}}{{\rm D}t} = -\boldsymbol{\nabla} \overline{p}_{\rm tot} + \mu_0^{-1} (\overline{\boldsymbol{B}} \cdot \boldsymbol{\nabla}) \overline{\boldsymbol{B}} + \overline{\rho} \boldsymbol{g} - \nu_{\rm t} \overline{\rho} \overline{\boldsymbol{Q}}, \tag{2}$$

$$0 = -\boldsymbol{\nabla} \cdot \overline{\rho}\, \overline{\boldsymbol{U}}, \tag{3}$$

where ${\rm D}/{\rm D}t = \partial/\partial t + \overline{\boldsymbol{U}} \cdot \boldsymbol{\nabla}$ is the advective derivative, $\overline{p}_{\rm tot} = \overline{p} + p_{\rm eff}$ is the mean total pressure, $\overline{p}$ is the mean gas pressure,

$$p_{\rm eff} = (1 - q_{\rm p}) \overline{\boldsymbol{B}}^2 / 2\mu_0 \tag{4}$$

is the effective magnetic pressure (Kleeorin et al. 1990, 1993, 1996), $\overline{\rho}$ is the mean density, $\overline{\boldsymbol{B}} = \boldsymbol{\nabla} \times \overline{\boldsymbol{A}} + \hat{\boldsymbol{z}} B_0$ is the mean magnetic field with an imposed constant field pointing in the z direction, $\overline{\boldsymbol{J}} = \boldsymbol{\nabla} \times \overline{\boldsymbol{B}} / \mu_0$ is the mean current density, μ_0 is the vacuum permeability, $\boldsymbol{g} = (0, 0, -g)$ is the gravitational acceleration, $\eta_{\rm t}$ is the turbulent magnetic diffusivity, $\nu_{\rm t}$ is the turbulent viscosity,

$$-\overline{\boldsymbol{Q}} = \nabla^2 \overline{\boldsymbol{U}} + \tfrac{1}{3} \boldsymbol{\nabla} \boldsymbol{\nabla} \cdot \overline{\boldsymbol{U}} + 2 \overline{\boldsymbol{\mathsf{S}}} \boldsymbol{\nabla} \ln \overline{\rho} \tag{5}$$

is a term appearing in the viscous force with

$$\mathsf{S}_{ij} = \tfrac{1}{2} (\overline{U}_{i,j} + \overline{U}_{j,i}) - \tfrac{1}{3} \delta_{ij} \boldsymbol{\nabla} \cdot \overline{\boldsymbol{U}} \tag{6}$$

being the traceless rate-of-strain tensor of the mean flow.

We adopt an isothermal equation of state with $p = \rho c_{\rm s}^2$, where $c_{\rm s} = {\rm const.}$ is the sound speed. In the absence of a magnetic field, the hydrostatic equilibrium solution is then given by $\overline{\rho} = \rho_0 \exp(-z/H_\rho)$, where $H_\rho = c_{\rm s}^2 / g$ is the density scale height.

2.1. Analytical estimates of growth rate of NEMPI

We linearize the mean-field Eqs. (1)–(3) around the equilibrium: $\overline{\boldsymbol{U}}_0 = \boldsymbol{0}$, $\overline{\boldsymbol{B}} = \overline{\boldsymbol{B}}_0 = {\rm const.}$ The equations for small perturbations (denoted by a tilde) can be rewritten in the form

$$\frac{\partial \tilde{\boldsymbol{B}}}{\partial t} = \boldsymbol{\nabla} \times \left(\tilde{\boldsymbol{U}} \times \overline{\boldsymbol{B}}_0 \right), \tag{7}$$

$$\boldsymbol{\nabla} \cdot \tilde{\boldsymbol{U}} = \frac{\tilde{U}_z}{H_\rho}, \tag{8}$$

$$\frac{\partial \tilde{\boldsymbol{U}}}{\partial t} = \frac{1}{\overline{\rho}} \left[\mu_0^{-1} (\overline{\boldsymbol{B}}_0 \cdot \boldsymbol{\nabla}) \tilde{\boldsymbol{B}} - \boldsymbol{\nabla} \tilde{p}_{\rm eff} \right], \tag{9}$$

where

$$\tilde{p}_{\rm tot} = \tilde{p}_{\rm eff} = \frac{2 \overline{B}_0 \tilde{B}_z}{\mu_0} \left(\frac{{\rm d}\mathcal{P}_{\rm eff}}{{\rm d}\beta^2} \right)_{\beta = \beta_0} \tag{10}$$

with $\beta = \overline{B} / B_{\rm eq}$ and $B_{\rm eq} = \sqrt{\mu_0 \overline{\rho}}\, u_{\rm rms}$ is the local equipartition field strength, and $u_{\rm rms}$ is assumed to be a constant in the present mean-field study. Here, the effective magnetic pressure is written in normalized form as

$$\mathcal{P}_{\rm eff}(\beta) \equiv \mu_0 p_{\rm eff} / B_{\rm eq}^2 = \tfrac{1}{2} \left[1 - q_{\rm p}(\beta) \right] \beta^2. \tag{11}$$

In this section, we neglect dissipative terms such as the turbulent viscosity term in the momentum equation and the turbulent magnetic diffusion term in the induction equation. We consider the axisymmetric problem, use cylindrical coordinates r, φ, z and introduce the magnetic vector potential and stream function:

$$\tilde{\boldsymbol{B}} = \boldsymbol{\nabla} \times \left(A \mathrm{e}_\varphi \right), \quad \overline{\rho}\, \tilde{\boldsymbol{U}} = \boldsymbol{\nabla} \times \left(\Psi \mathrm{e}_\varphi \right). \tag{12}$$

Using the radial component of Eqs. (7) and (9) we arrive at the following equation for the function $\Phi(t, r, z) = \overline{\rho}^{-1} \nabla_z \Psi$:

$$\frac{\partial^2 \Phi}{\partial t^2} = v_{\rm A}^2(z) \left[\nabla_z^2 + 2 \left(\frac{{\rm d}\mathcal{P}_{\rm eff}}{{\rm d}\beta^2} \right)_{\beta = \beta_0} \Delta_{\rm s} \right] \Phi, \tag{13}$$

where $v_{\rm A}(z) = \overline{B}_0 / \sqrt{\mu_0 \overline{\rho}(z)}$ is the mean Alfvén speed, $\Delta_{\rm s}$ is the radial part of the Stokes operator,

$$\Delta_{\rm s} = \frac{1}{r} \frac{\partial}{\partial r} \left(r \frac{\partial}{\partial r} \right) - \frac{1}{r^2},$$

and we have used an exponential profile for the density stratification in an isothermal layer,

$$\overline{\rho} = \overline{\rho}_0 \exp(-z/H_\rho). \tag{14}$$

We seek solutions of Eq. (13) in the form

$$\Phi(t, r, z) = \exp(\lambda t)\, J_1(\sigma r / R)\, \Phi_0(z), \tag{15}$$

where $J_1(x)$ is the Bessel function of the first kind, which satisfies the Bessel equation: $\Delta_s J_1(ar) = -a^2 J_1(ar)$. Substituting Eq. (15) into Eq. (13), we obtain the equation for the function $\Phi_0(z)$:

$$\frac{{\rm d}^2 \Phi_0}{{\rm d}z^2} - \left[\frac{\lambda^2}{v_{\rm A}^2(z)} + \frac{2\sigma^2}{R^2} \left(\frac{{\rm d}\mathcal{P}_{\rm eff}}{{\rm d}\beta^2} \right)_{\beta = \beta_0} \right] \Phi_0 = 0. \tag{16}$$

For $R^2 \Phi_0''(z) / \Phi_0 \ll 1$, the growth rate of NEMPI is given by

$$\lambda = \frac{v_{\rm A} \sigma}{R} \left[-2 \left(\frac{{\rm d}\mathcal{P}_{\rm eff}}{{\rm d}\beta^2} \right)_{\beta = \beta_0} \right]^{1/2}. \tag{17}$$

This equation shows that, compared to the case of a horizontal magnetic field, where there was a factor H_ρ in the denominator, in the case of a vertical field the relevant length is R/σ. Introducing as a new variable $X = \beta_0^2(z)$, we can rewrite Eq. (16) in the form

$$X^3 \frac{{\rm d}^2 \Phi_0}{{\rm d}X^2} + X^2 \frac{{\rm d}\Phi_0}{{\rm d}X} - \left(\frac{\lambda^2 H_\rho^2}{u_{\rm rms}^2} + \frac{2\sigma^2 H_\rho^2}{R^2} X \frac{{\rm d}\mathcal{P}_{\rm eff}}{{\rm d}X} \right) \Phi_0 = 0. \tag{18}$$

We now need to make detailed assumptions about the functional form of $\mathcal{P}_{\rm eff}(\beta^2)$. A useful parameterization of $q_{\rm p}$ in Eq. (4) is (Kemel et al. 2012b)

$$q_{\rm p} = \frac{q_{\rm p0}}{1 + \beta^2 / \beta_{\rm p}^2} \equiv \frac{\beta_\star^2}{\beta_{\rm p}^2 + \beta^2}, \tag{19}$$

where $\beta_\star = \sqrt{q_{\rm p0}} \beta_{\rm p}$. It is customary to obtain approximate analytic solutions to Eq. (18) as marginally bound states of the associated Schrödinger equation, $\Psi_0'' - \tilde{U}(X)\, \Psi_0 = 0$, via the transformation $\Phi_0 = \Psi_0 / \sqrt{X}$, where

$$\tilde{U}(X) = \frac{\lambda^2 H_\rho^2}{u_{\rm rms}^2 X^3} - \frac{1}{4X^2} + \frac{\sigma^2 H_\rho^2}{R^2 X^2} \left(1 - \frac{q_{\rm p0}}{(1 + X^2 / \beta_{\rm p}^2)^2} \right), \tag{20}$$

where primes denote a derivative with respect to X. The potential $\tilde{U}(X)$ has the following asymptotic behavior: $\tilde{U} \to \lambda^2 H_\rho^2 / (u_{\rm rms}^2 X^3)$ for small X, and $\tilde{U}(X) \to (\sigma^2 H_\rho^2 / R^2 - 1/4) X^{-2}$ for large X. For the existence of an instability, the potential $\tilde{U}(R)$ should have a negative minimum. However, the exact values of the growth rate of NEMPI, the scale at which the growth rate attains the maximum value, and how the resulting magnetic field structure looks like in the nonlinear saturated regime of NEMPI can only be obtained numerically using MFS.

2.2. MFS models

For consistency with earlier studies, we keep the governing MFS parameters equal to those used in a recent study by Losada et al. (2013). Thus, unless stated otherwise, we use the values

$$q_{\rm p0} = 32, \quad \beta_{\rm p} = 0.058 \quad \text{(reference model)}, \tag{21}$$

which are based on Eq. (22) of Brandenburg et al. (2012), applied to $\mathrm{Re}_M = 18$.

The mean-field equations are solved numerically without making the anelastic approximation, i.e., we solve

$$\frac{\partial \overline{\rho}}{\partial t} = -\boldsymbol{\nabla}\cdot\overline{\rho}\,\overline{\boldsymbol{U}} \tag{22}$$

together with the equations for the mean vector potential $\overline{\boldsymbol{A}}$ such that $\overline{\boldsymbol{B}} = \boldsymbol{B}_0 + \boldsymbol{\nabla}\times\overline{\boldsymbol{A}}$ is divergence-free, the mean velocity $\overline{\boldsymbol{U}}$, and the mean density $\overline{\rho}$, using the Pencil Code[1], which has a mean-field module built in and is used for calculations both in Cartesian and cylindrical geometries. Here, $\boldsymbol{B}_0 = (0, 0, B_0)$ is the imposed uniform vertical field. The respective coordinate systems are (x, y, z) and (r, φ, z). In the former case we use periodic boundary conditions in the horizontal directions, $-L_\perp/2 < (x, y) < L_\perp/2$, while in the latter we adopt perfect conductor, free-slip boundary conditions at the side walls at $r = L_r$ and regularity conditions on the axis. On the upper and lower boundaries at $z = z_{\rm top}$ and $z = z_{\rm bot}$ we use in both geometries stress-free conditions, $\hat{\boldsymbol{z}}\times\partial\overline{\boldsymbol{U}}/\partial z = \boldsymbol{0}$ and $\hat{\boldsymbol{z}}\cdot\overline{\boldsymbol{U}} = 0$, and assume the magnetic field to be normal to the boundary, i.e., $\hat{\boldsymbol{z}}\times\overline{\boldsymbol{B}} = \boldsymbol{0}$.

Following earlier work, we display results for the magnetic field either by normalizing with B_0, which is a constant, or by normalizing with $B_{\rm eq}$, which decreases with height. The strength of the imposed field is often specified in terms of $B_{\rm eq0} = B_{\rm eq}(z = 0)$.

2.3. Nondimensionalization

Nondimensional parameters are indicated by tildes and hats, and include $\tilde{B}_0 = B_0/(\mu_0\rho_0 c_{\rm s}^2)^{1/2}$ and $\tilde{\eta}_{\rm t} = \eta_{\rm t}/c_{\rm s}H_\rho$, in addition to parameters in Eq. (21) characterizing the functional form of $q_{\rm p}(\beta)$. Additional quantities include $\tilde{k}_{\rm f} = k_{\rm f}H_\rho$ and $\hat{k}_{\rm f} = k_{\rm f}/k_1$, where a hat is used to indicate nondimensionalization that uses quantities other than $c_{\rm s}$ and H_ρ, such as $k_1 = 2\pi/L_\perp$, which is the lowest horizontal wavenumber in a domain with horizontal extent $L_\perp$. For example, $\hat{g} = g/c_{\rm s}^2 k_1$, is nondimensional gravity and $\hat{\lambda} = \lambda H_\rho^2/\eta_{\rm t}$ is the nondimensional growth rate. It is convenient to quote also $B_0/B_{\rm eq0}$ with $B_{\rm eq0} = B_{\rm eq}(z = 0)$. Note that $B_0/B_{\rm eq0}$ is larger than $\tilde{B}_0$ by the inverse of the turbulent Mach number, $\mathrm{Ma} = u_{\rm rms}/c_{\rm s}$. It is convenient to normalize the mean flow by $u_{\rm rms}$ and denote it by a hat, i.e., $\hat{\overline{U}} = \overline{U}/u_{\rm rms}$. Likewise, we define $\hat{\overline{B}} = \overline{B}/B_{\rm eq}$.

In MFS, the value of $\eta_{\rm t}$ is assumed to be given by $\eta_{\rm t0} = u_{\rm rms}/3k_{\rm f}$. Using the test-field method, Sur et al. (2008) found this to be an accurate approximation of $\eta_{\rm t}$. Thus, we have to specify both Ma and $\tilde{k}_{\rm f}$. In most of our runs we use $\mathrm{Ma} = 0.1$ and $\tilde{k}_{\rm f} = 33$, corresponding to $\tilde{\eta}_{\rm t} = 10^{-3}$. Furthermore, $k_{\rm f}$ and H_ρ are in principle not independent of each other either. In fact, mixing length theory suggests $k_{\rm f}H_\rho \approx 6.5$ (Losada et al. 2013), but it would certainly be worthwhile to compute this quantity from high-resolution convection simulations spanning multiple scale heights. However, in this paper, different values of $k_{\rm f}H_\rho$ are considered. With these preparations in place, we can now address questions concerning the horizontal wavelength of the instability and the vertical structure of the magnetic flux tubes.

[1] http://pencil-code.googlecode.com

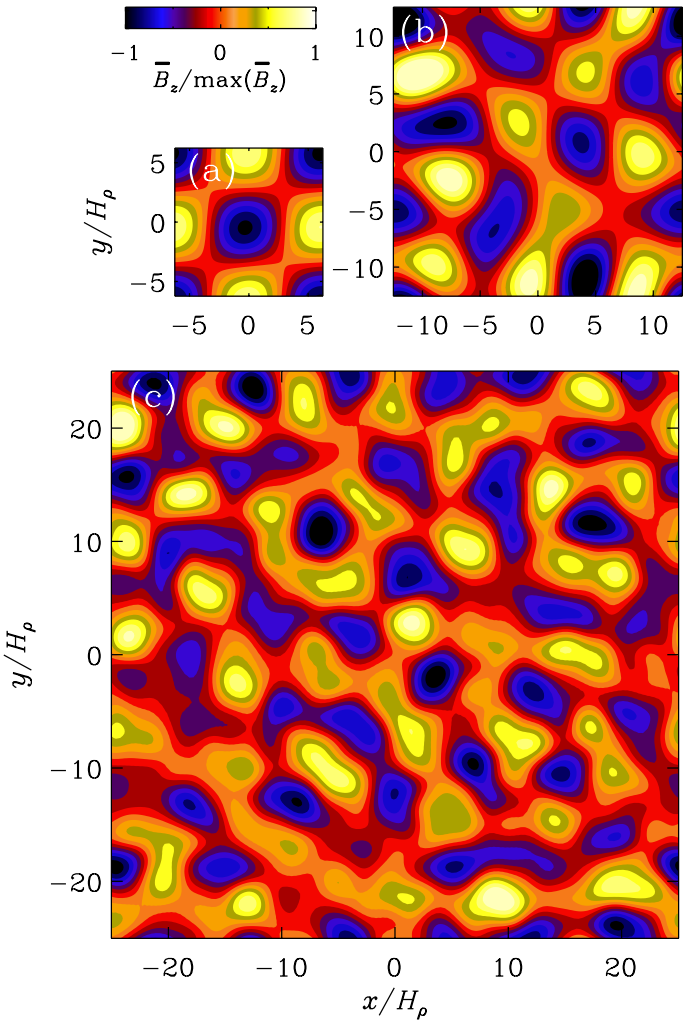

Fig. 1. Horizontal patterns of $\overline{B}_z$ at $z = 0$ from a 3D MFS during the kinematic growth phase with $B_0/B_{\rm eq0} = 0.1$ and horizontal extents with **a)** $L_\perp/H_\rho = 4\pi$; **b)** 8π; and **c)** 16π.

2.4. Aspect ratio of NEMPI

The only natural length scale in an isothermal layer in MFS is H_ρ. It determines the scale of NEMPI. At onset, the horizontal scale of the magnetic field pattern will be a certain multiple of H_ρ. In the following we denote the corresponding horizontal wavenumber of this pattern by $k_\perp$. Earlier work by Kemel et al. (2013) showed that for an imposed horizontal magnetic field we have $k_\perp H_\rho \approx 0.8...1$. This pattern was 2D in the plane perpendicular to the direction of the imposed magnetic field, corresponding to horizontal rolls oriented along the mean magnetic field. In the present case of a vertical field, the magnetic perturbations have a cellular pattern with horizontal wavenumber $k_\perp$. To determine the value of $k_\perp H_\rho$ for the case of an imposed vertical magnetic field, we have to ensure that the number of cells per unit area is independent of the size of the domain. In Fig. 1, we compare MFS with horizontal aspect ratios ranging from 2 to 8. We see that the magnetic pattern is fully captured in a domain with normalized horizontal extent $L_\perp/H_\rho = 4\pi$, i.e., the horizontal scale of the magnetic field pattern is twice the value of H_ρ,

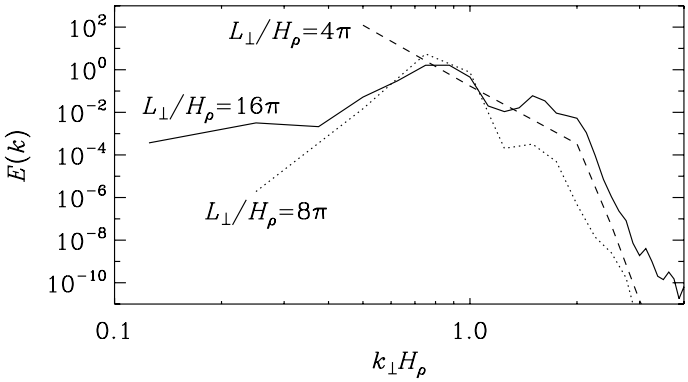

Fig. 2. Power spectra of $\overline{B}_z$ for different horizontal domain sizes at $z = 0$ from a 3D MFS during the kinematic growth phase with $B_0/B_{\rm eq0} = 0.1$.

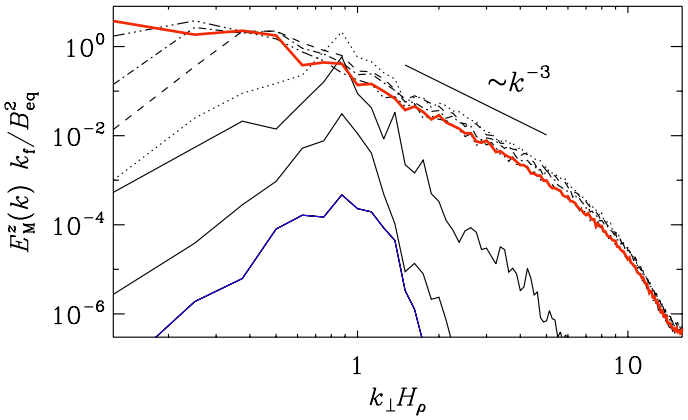

Fig. 3. Time evolution of normalized spectra of B_z from 3D MFS during the late nonlinear phase at the top of the domain, $k_1 z = \pi$, at normalized times $t\eta_{\rm t0}/H_\rho^2 \approx 5$ (blue), 6, 7, 10, 20, 30, 40, and 50 (red), with $g = c_{\rm s}^2 k_1$, $B_0/B_{\rm eq0} = 0.1$, and $L_\perp/H_\rho = 16\pi$.

i.e., $k_x = k_y = H_\rho^{-1}/2$, so that $k_\perp \equiv (k_x^2 + k_y^2)^{1/2} = H_\rho^{-1}/\sqrt{2}$, or $k_\perp H_\rho \approx 0.7$. The value $k_\perp H_\rho \approx 0.7$ is also confirmed by taking a power spectrum of $\overline{B}_z(x, y)$; see Fig. 2, which shows a peak at a similar value.

Comparing the three simulations shown in Fig. 1, we see that a regular checkerboard pattern is only obtained for the smallest domain size; see Fig. 1a. For larger domain sizes the patterns are always irregular such that a cell of one sign can be surrounded by 3–5 cells of the opposite sign. Nevertheless, in all three cases we have approximately the same number of cells per unit area.

In the nonlinear regime, structures continue to merge and more power is transferred to lower horizontal wavenumbers; see Fig. 3. Later in Sect. 3.5 we present similar results also for our DNS.

2.5. Vertical magnetic field profile during saturation

In an isothermal atmosphere, the scale height is constant and there is no physical upper boundary, so we can extend the computation in the z direction at will, although the magnetic pressure will strongly exceed the turbulent pressure at large heights, which can pose computational difficulties. To study the full extent of magnetic flux concentrations, we need a big enough domain. In the following we consider the range $-3\pi \le z/H_\rho \le 3\pi$, which results in a density contrast of more than 10^8. To simplify matters, we restrict ourselves in the present study to axisymmetric calculations which are faster than 3D Cartesian ones.

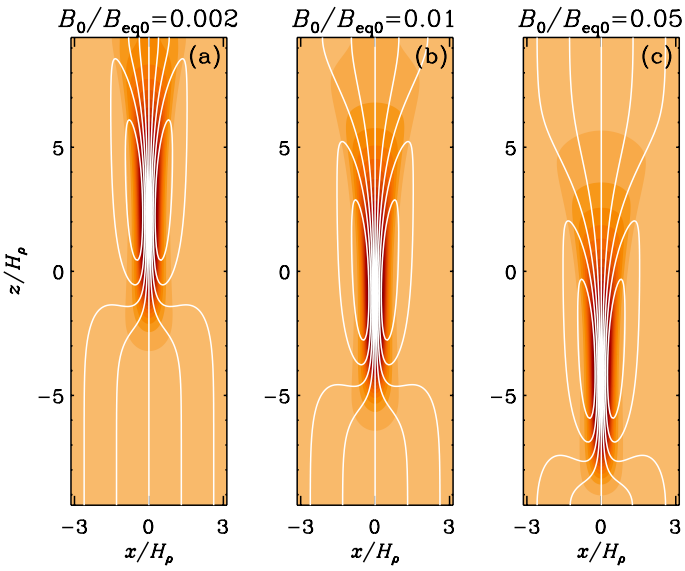

Fig. 4. Comparison of magnetic field profiles from axisymmetric MFS for Runs Bv002/33–Bv05/33 with three values of $B_0/B_{\rm eq0}$ and $\tilde{\eta}_{\rm t} = 10^{-3}$, corresponding to $k_{\rm f} H_\rho = 33$.

In Fig. 4 we compare the results for the mean magnetic field profiles for three values of $B_0/B_{\rm eq0}$ ranging from 0.002 to 0.05. These values are smaller than those studied in Sect. 2.4, because in the nonlinear regime and in a deeper domain the structures are allowed to sink by a substantial amount. By choosing $B_0/B_{\rm eq0}$ to be smaller, the tubes are fully contained in our domain. As B_0 increases, we expect the position of the magnetic flux tube, z_B, to move downward like

$$z_B = z_{B0} - 2H_\rho \ln(B_0/B_{\rm eq0}), \tag{23}$$

where $z_{B0} = 2H_\rho \ln \beta_0^{\rm opt}$ is a reference height and

$$\beta_0^{\rm opt} \equiv B_0/B_{\rm eq}(z_B) \approx 0.03...0.06 \tag{24}$$

is the optimal normalized field strength for NEMPI to be excited (Losada et al. 2013). The validity of Eq. (23) can be verified through Fig. 4, where $B_0/B_{\rm eq0}$ increases by a factor of 25, corresponding to $\Delta z_B = -6.4$.

In all cases, we obtain a slender tube with approximate aspect ratio of 1:8. In other words, the shape of the magnetic field lines is the same for all three values of $B_0/B_{\rm eq0}$, and just the position of the magnetic flux concentration shifts in the vertical direction. Note in particular that the thickness of structures is always the same. This is different from the nonlinear MFS in Cartesian geometry discussed above, where structures are able to merge. Merging is not really possible in the same way in an axisymmetric container, because any additional structure would correspond to a ring.

The mean flow structure associated with the magnetic flux tube is shown in Fig. 5 for Run Bv05/33 with $B_0/B_{\rm eq0} = 0.05$. We find inflow into the tube along field lines at large heights and outflow at larger depth. The vertical component of the flow in the tube points always downward, i.e., there is no obvious effect from positive magnetic buoyancy. The maximum downflow speed is about $0.27 u_{\rm rms}$, so it is subdominant compared with the turbulent velocity, but this could be enough to cause a noticeable temperature change in situations where the energy equation is solved.

The resulting magnetic field lines look roughly similar to those of the DNS with an imposed vertical magnetic field

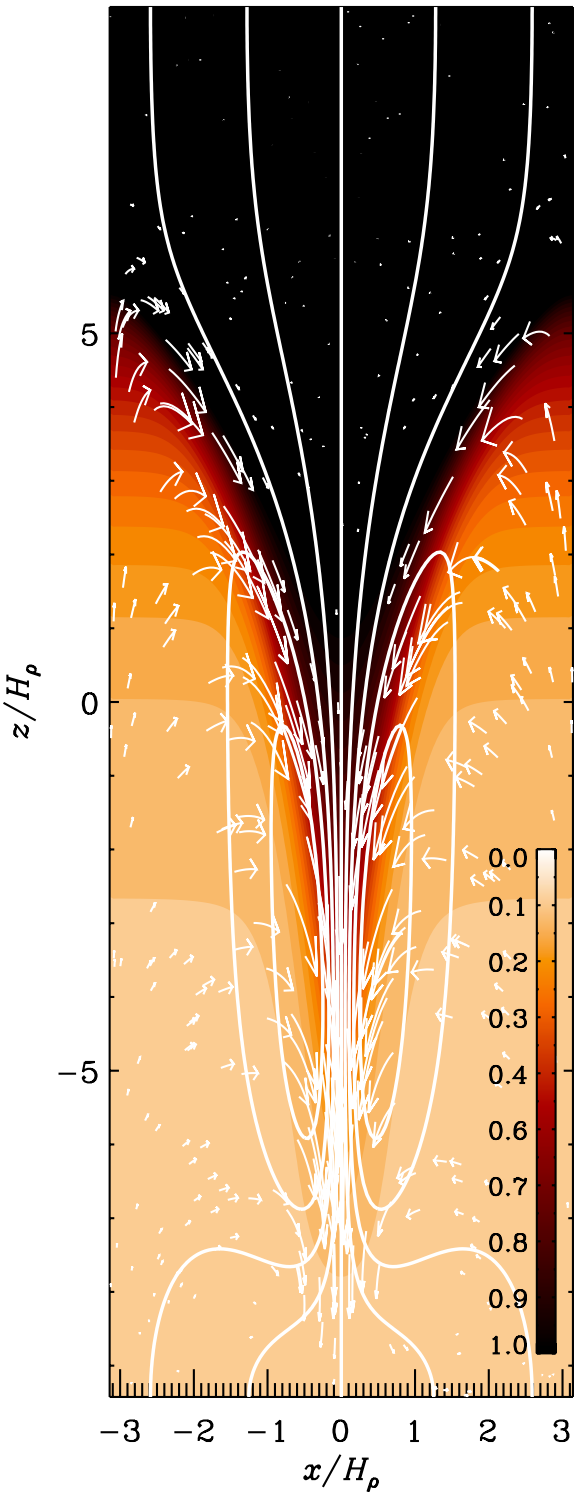

Fig. 5. $\overline{B}_z/B_{\rm eq}$ together with field lines and flow vectors from MFS, for Run Bv05/33 with $B_0/B_{\rm eq0} = 0.05$. The flow speed varies from $-0.27u_{\rm rms}$ (downward) to $0.08u_{\rm rms}$ (upward).

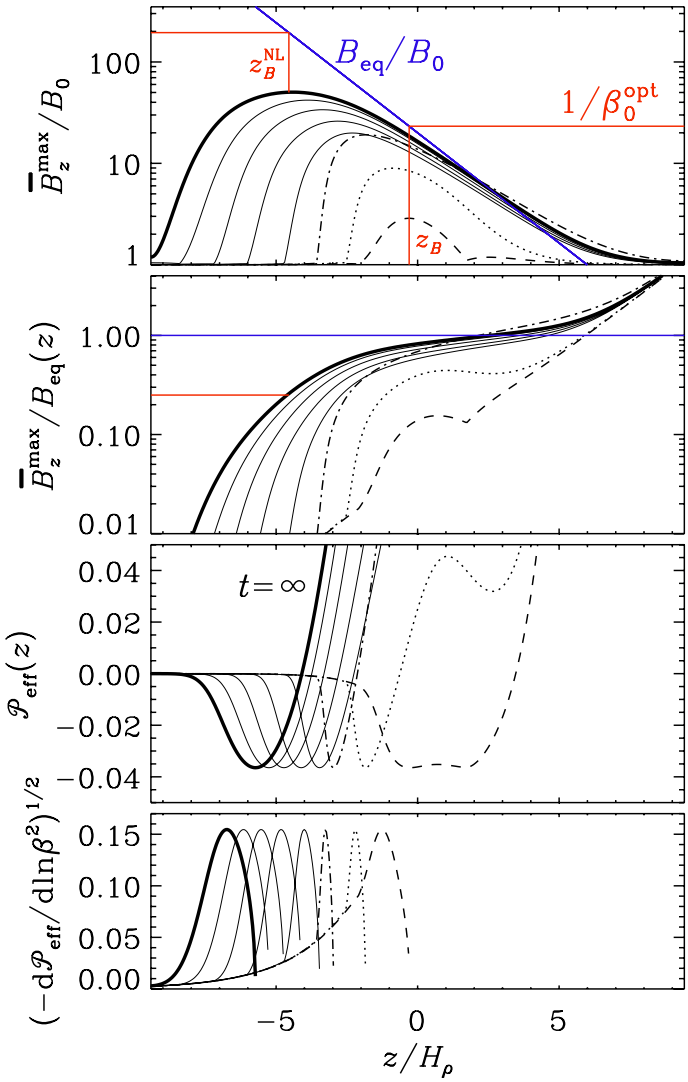

Fig. 6. Time evolution of normalized vertical magnetic field profiles, **a)** $\overline{B}_z^{\rm max}/B_0$ together with $B_{\rm eq}(z)/B_0$ (shown by blue line), **b)** $\overline{B}_z^{\rm max}/B_{\rm eq}(z)$; as well as **c)** $\mathcal{P}_{\rm eff}(z)$ and **d)** $(-{\rm d}\mathcal{P}_{\rm eff}/{\rm d}\ln\beta^2)^{1/2}$, from a MFS for Run Bv05/33 with $B_0/B_{\rm eq0} = 0.05$ at $t/\tau_{\rm td} = 2.9$ (dashed), 3 (dotted), 3.1 (dash-dotted), 3.3, 3.7, 4.2., 5, and 50 (thick solid line). The blue solid lines indicate $B_{\rm eq}(z)$, normalized by **a)** B_0 and **b)** by itself (corresponding thus to unity). The red lines indicate the locations z_B and $z_B^{\rm NL}$, as well as relevant intersections with normalized values of $\overline{B}_z^{\rm max}$ and $B_{\rm eq}$.

(Brandenburg et al. 2013). In DNS, however, the thickness of the magnetic flux tube is larger than in the MFS by about a factor of three. This discrepancy could be explained if the actual value of $\eta_{\rm t}$ was in fact larger than the estimate given by $\eta_{\rm t0}$. We return to this possibility in Sect. 3.5. Alternatively, it might be related to the possibility that the coefficients in Eq. (21) could actually be different.

The time evolution of the vertical magnetic field profiles, $\overline{B}_z^{\rm max}/B_0$ and $\overline{B}_z^{\rm max}/B_{\rm eq}(z)$, is shown in Fig. 6 at different times for the case $B_0/B_{\rm eq0} = 0.05$, corresponding to Fig. 4c. Here, we also show the time evolution of the corresponding profiles of $\mathcal{P}_{\rm eff}(z)$ and $(-{\rm d}\mathcal{P}_{\rm eff}/{\rm d}\ln\beta^2)^{1/2}$. In the kinematic regime, the peak of the latter quantity is a good indicator of the peak of the eigenfunction (Kemel et al. 2013). In the present case, the magnetic field in the kinematic phase peaks at a height z_B that is given by the condition (24). According to the MFS of Losada et al. (2013), this condition is approximately the same for vertical and horizontal fields. Looking at Fig. 6 for $B_0/B_{\rm eq0} = 0.05$, we see that at $z/H_\rho \approx -0.5$ we have $B_{\rm eq}/B_0 \approx 33$, which agrees with Eq. (24). However, unlike the case of a horizontal magnetic field, where in the kinematic phase the mean field was found to peak at a height below that where $(-{\rm d}\mathcal{P}_{\rm eff}/{\rm d}\ln\beta^2)^{1/2}$ peaks, we now see that the field peaks above that position.

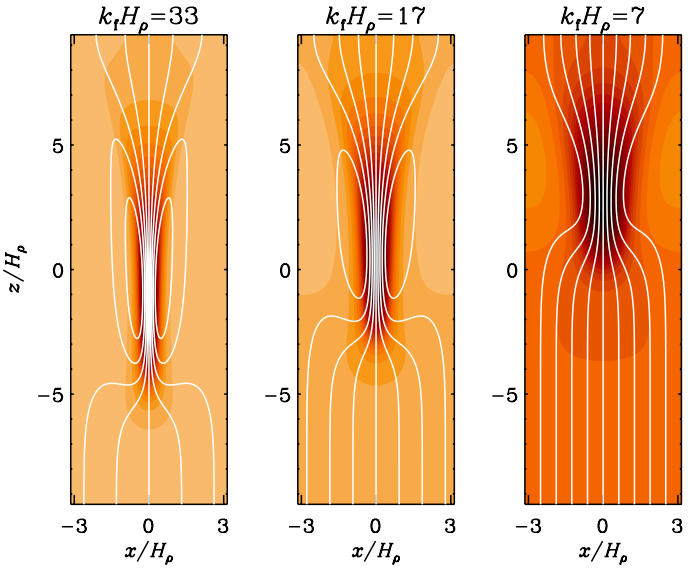

Fig. 7. Comparison of magnetic field profiles from an axisymmetric MFS for Runs Bv01/33–Bv01/7 with $B_0/B_{\rm eq0} = 0.01$ and three values of k_fH_ρ.

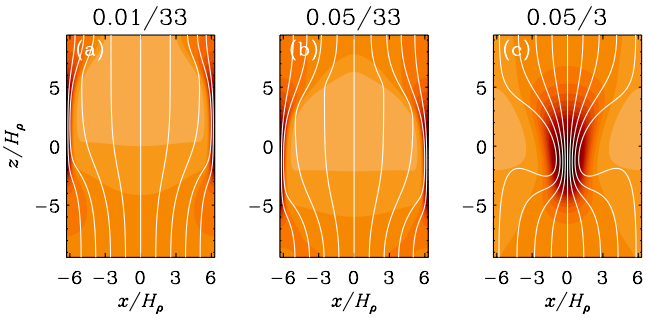

Fig. 8. Comparison of magnetic field structure in axisymmetric MFS. **a)** Run 0.01/33 with $B_0/B_{\rm eq0} = 0.01$ and **b)** Run 0.05/33 with $B_0/B_{\rm eq0} = 0.05$, both with $k_fH_\rho = 33$. The flow speeds vary from $-0.27u_{\rm rms}$ to $0.08u_{\rm rms}$ in both cases. **c)** Run 0.05/3 with $B_0/B_{\rm eq0} = 0.05$ and $k_fH_\rho = 3$. The flow speed varies from $-0.23u_{\rm rms}$ to $0.07u_{\rm rms}$.

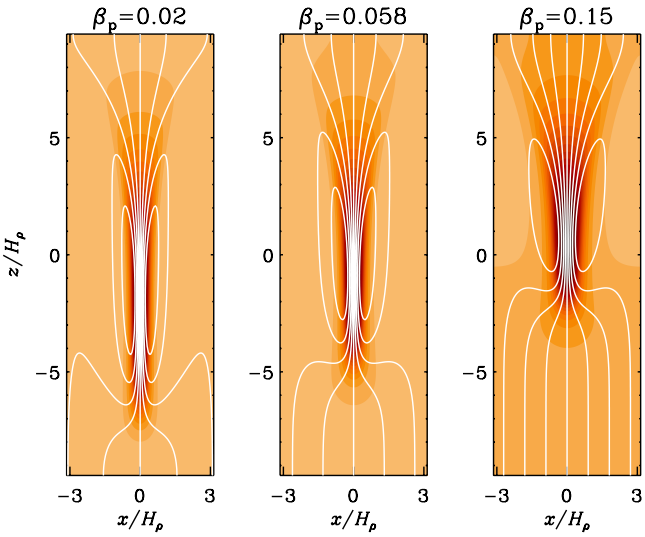

Fig. 9. Comparison of magnetic field structure in axisymmetric MFS for Runs Bu01/33–Bw01/33 with three values of $\beta_{\rm p}$.

As NEMPI begins to saturate, the peak of $\overline{B}_z^{\rm max}$ moves further down to $z = z_B^{\rm NL} \approx -5\,H_\rho$ during the next one or two turbulent diffusive times. By that time, $\overline{B}_z^{\rm max}$ has reached values up to $\overline{B}_z^{\rm max}/B_0 \approx 50$. At that depth, $\overline{B}_z^{\rm max}/B_{\rm eq}(z)$ is about 0.25, but this quantity continues to increase with height and reaches super-equipartition values at $z/H_\rho \approx 3$ (second panel of Fig. 6).

2.6. Smaller scale separation

In MFS, as noted above, the wavenumber of turbulent eddies, $k_{\rm f}$, enters the expression for the turbulent diffusivity via $\eta_{\rm t} \approx u_{\rm rms}/3k_{\rm f}$, and thus $\tilde{\eta}_{\rm t} \approx {\rm Ma}/3\tilde{k}_{\rm f}$, so we have

$$\tilde{k}_{\rm f} \equiv k_{\rm f}H_\rho = H_\rho^2/3\tau\eta_{\rm t} = {\rm Ma}/3\tilde{\eta}_{\rm t}, \tag{25}$$

where $\tau = H_\rho/u_{\rm rms}$ is the turnover time per scale height. When $u_{\rm rms}$ is kept unchanged, smaller scale separation implies a decrease of $\tilde{k}_{\rm f}$, i.e., the size of turbulent eddies in the domain is increased. Earlier work has indicated that the growth rate of the instability for horizontal magnetic field decreases with decreasing $\tilde{k}_{\rm f}$ (Brandenburg et al. 2012). However, we do not know whether this also causes a change in the spot diameter, which would be plausible, or a change in the depth at which NEMPI occurs. In our MFS we have chosen ${\rm Ma} = 0.1$ and $\tilde{\eta}_{\rm t}$ corresponds to $\tilde{k}_{\rm f} \approx 33$. For $\tilde{\eta}_{\rm t} = 5\times10^{-3}$ we have $\tilde{k}_{\rm f} \approx 7$, which is about the smallest scale separation for which NEMPI is still possible in this geometry; see Fig. 7. Interestingly, as $\tilde{k}_{\rm f}$ is decreased, the location of the flux tube structure moves upward. This can be understood as a consequence of enhanced turbulent diffusion, which makes the flux tubes less concentrated, so the magnetic field is weaker, but weaker magnetic field sinks less than stronger fields.

Even for $k_{\rm f}H_\rho \approx 3$ it is still possible to find NEMPI in MFS, but, as we have seen, the flux tube moves upward and becomes thicker. To accommodate for this change, we need to increase the diameter of the domain and, in addition, we would either need to extend it in the upward direction or increase the magnetic field strength to move the tube back down again; cf. Fig. 4. We choose here the latter. In Fig. 8, we show three cases for a wider box. In the first two runs (referred to as "0.01/33" and "0.05/33") we keep the scale separation ratio the same as before, i.e. $\tilde{k}_{\rm f} = 33$, and increase $B_0/B_{\rm eq0}$ from 0.01 to 0.05, while in the third case we keep $B_0/B_{\rm eq0} = 0.05$ and decrease $\tilde{k}_{\rm f}$ to 3. We increase the magnetic field by a factor of 5 so as to keep the structure within the computational domain. In the first case, the natural separation between tubes would be too small for this large cylindrically symmetric container. By contrast, in a 3D Cartesian domain, a second downdraft would form, which is not possible in an axisymmetric geometry. Instead, a downdraft develops on the outer rim of the container. On the other hand, if $\tilde{k}_{\rm f}$ is decreased and thus $\tilde{\eta}_{\rm t}$ increased, a single downdraft is again possible, as shown in Fig. 8b, suggesting that the horizontal scale of structures is also increased as $\tilde{\eta}_{\rm t}$ is increased. We see that the tube can now attain significant diameters. Its height remains unchanged, so the aspect ratio of the structure is decreased as the scale separation ratio is decreased.

2.7. Parameter sensitivity

It is important to know the dependence of the solutions on changes of the parameters $\beta_{\rm p}$ and $\beta_\star$ that determine the function $q_{\rm p}$. In Figs. 9 and 10, we present results where we change either $\beta_{\rm p}$ or $\beta_\star$, respectively. Characteristic properties of these solutions are summarized in Table 1. Runs Ov002/33–Ov05/33

Table 1. Survey of axisymmetric MFS giving normalized growth rates, mean field strengths, mean flow speeds, and other properties for different values of $\beta_0, \beta_\star, \beta_p$, and $\tilde{k}_f$.

Run	β_0	q_{p0}	$\beta_\star$	β_p	β_{min}	$\mathcal{P}_{eff}^{min}$	$\tilde{k}_f$	$\hat{\lambda}$	$\hat{\overline{B}}_z^{max}$	$\hat{\overline{U}}_z^{min}$	$\hat{\overline{U}}_z^{max}$	$\tilde{z}_B$	$\tilde{z}_B^{NL}$	$\tilde{Z}_b$	$\tilde{Z}_t$	$\tilde{R}$	A
Ov002/33	0.002	32	0.33	0.058	0.125	−0.036	33	5.0	52	−0.27	0.03	8.3	4.8	3.5	4.6	0.27	17
Ov01/33	0.01	32	0.33	0.058	0.125	−0.036	33	5.6	52	−0.27	0.08	5.0	1.6	3.6	4.3	0.27	16
Ov05/33	0.05	32	0.33	0.058	0.125	−0.036	33	2.2	51	−0.27	0.08	1.7	−1.7	3.7	4.3	0.27	16
Bv002/33	0.002	32	0.33	0.058	0.125	−0.036	33	7.6	52	−0.27	0.03	7.9	2.0	3.1	4.1	0.35	12
Bv01/33	0.01	32	0.33	0.058	0.125	−0.036	33	9.4	52	−0.27	0.08	3.9	−1.2	3.1	4.1	0.35	12
Bv05/33	0.05	32	0.33	0.058	0.125	−0.036	33	12.3	51	−0.27	0.08	1.8	−4.4	3.0	4.1	0.35	12
Bv01/33	0.01	32	0.33	0.058	0.125	−0.036	33	9.4	52	−0.27	0.08	4.8	−1.2	3.1	4.1	0.35	12
Bv01/17	0.01	32	0.33	0.058	0.125	−0.036	17	2.1	25	−0.27	0.08	4.9	0.3	2.8	4.1	0.50	8
Bv01/7	0.01	32	0.33	0.058	0.125	−0.036	7	0.4	8	−0.23	0.07	4.7	2.7	2.4	3.8	0.95	4
Bu01/33	0.01	270	0.33	0.02	0.079	−0.048	33	5.1	69	−0.35	0.10	4.5	−2.1	4.0	4.5	0.30	15
Bv01/33	0.01	32	0.33	0.058	0.125	−0.036	33	9.4	52	−0.27	0.08	4.8	−1.2	3.1	4.1	0.35	12
Bw01/33	0.01	4.8	0.33	0.15	0.164	−0.016	33	3.2	25	−0.15	0.05	5.4	0.3	2.2	3.8	0.50	8
Av01/33	0.01	12	0.2	0.058	0.091	−0.010	33	2.6	22	−0.13	0.04	4.3	−0.3	2.3	3.8	0.55	7
Bv01/33	0.01	32	0.33	0.058	0.125	−0.036	33	9.4	52	−0.27	0.08	4.8	−1.2	3.1	4.1	0.35	12
Cv01/33	0.01	74	0.5	0.058	0.160	−0.097	33	10.6	91	−0.47	0.09	5.4	−1.7	3.5	4.3	0.25	17
Av01/33*	0.01	12	0.2	0.058	0.091	−0.010	33	2.4	11	−0.07	0.04	4.2	1.6	1.4	3.4	0.85	4
Bv01/33*	0.01	32	0.33	0.058	0.125	−0.036	33	4.8	21	−0.15	0.08	4.7	1.5	1.3	3.3	0.60	5
Cv01/33*	0.01	74	0.5	0.058	0.160	−0.097	33	8.7	33	−0.26	0.10	5.3	1.4	1.2	3.2	0.50	6

Notes. In all cases we have $k_1 H_\rho = 1$, so $\tilde{k}_f = \hat{k}_f$. Asterisks indicate that the domain was clipped at $z_{bot} = 0$.

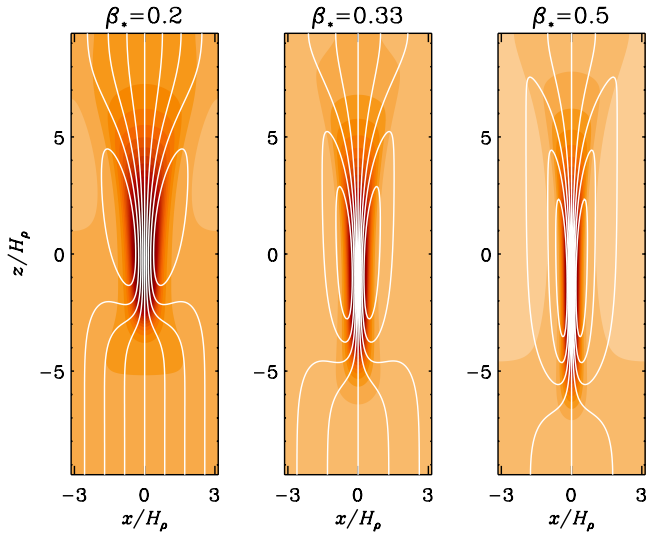

Fig. 10. Comparison of magnetic field structure in axisymmetric MFS for Runs Av01/33–Cv01/33 three values of $\beta_\star$.

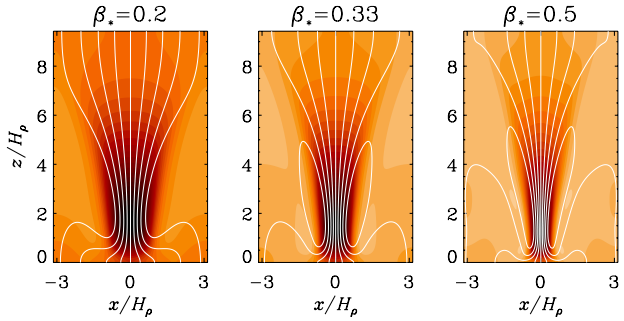

Fig. 11. Comparison of magnetic field structure in axisymmetric MFS for Runs Av–Cv01/33* with three values of $\beta_\star$ in a domain that is truncated from below.

are 2D Cartesian while all other ones are 2D axisymmetric. In addition to β_p and $\beta_\star$, we also list the values of $q_{p0} = \beta_\star^2/\beta_p^2$, as well as the minimum position of the $\mathcal{P}_{eff}(\beta)$ curve, namely (cf. Kemel et al. 2012b)

$$\mathcal{P}_{eff}^{min} = -\tfrac{1}{2}(\beta_\star^2 - \beta_p^2)^2, \quad \beta_{min} = \left(\beta_p \sqrt{-2\mathcal{P}_{eff}^{min}}\right)^{1/2}. \tag{26}$$

The main output parameters include the normalized growth rate in the linear regime, $\hat{\lambda} = \lambda H_\rho^2/\eta_t$, the maximum normalized vertical field in the tube

$$\hat{\overline{B}}_z^{max} = \overline{B}_z^{max} \Big/ B_0, \tag{27}$$

the minimum and maximum normalized velocities,

$$\hat{\overline{U}}_z^{min} = \overline{U}_z^{min} \Big/ u_{rms}, \qquad \hat{\overline{U}}_z^{max} = \overline{U}_z^{max} \Big/ u_{rms}, \tag{28}$$

the normalized maximum magnetic field positions in the linear and nonlinear regimes, $\tilde{z}_B = z_B/H_\rho$ and $\tilde{z}_B^{NL} = z_B^{NL}/H_\rho$, respectively, the similarly normalized positions where $\overline{B}_z$ has dropped by $1/e$ of its maximum at the bottom end $\tilde{Z}_b$, at the top end $\tilde{Z}_t$, and to the side $\tilde{R}$ of the tube, as well as the aspect ratio $A = Z_t/R$.

The changes of $\hat{\lambda}$ are often as expected: a decrease with decreasing values of $\tilde{k}_f$, and a increase with increasing values of $\beta_\star$. There are also some unexpected changes that could be associated with the tube not being fully contained within our fixed domain: for Run Ov05/33 the domain may not be deep enough and for Run Bw01/33 it may not be wide enough. Furthermore, we find that structures become taller when β_p is small and $\beta_\star$ large, and they become shorter and fatter when β_p is large and $\beta_\star$ small. Thus, thicker structures, as indicated by the DNS of Brandenburg et al. (2013), could also be caused by larger values of β_p or smaller values of $\beta_\star$. When the domain is clipped at $z = 0$, flux concentrations cannot fully develop. The structures are fatter and less strong; see Fig. 11.

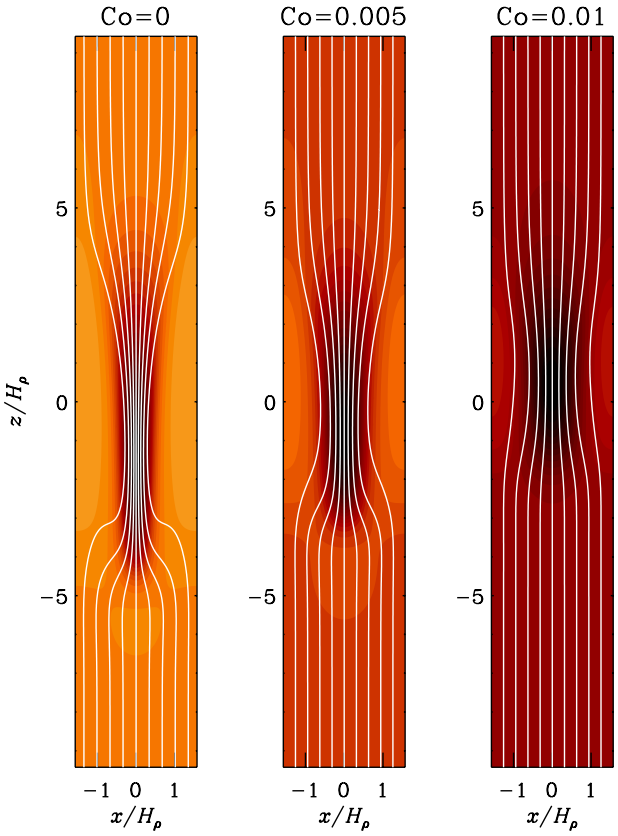

Fig. 12. Comparison of magnetic field structure in axisymmetric MFS for a run similar to Run Bv01/33, but for three values of Co and $r/H_\rho \le \pi/2$.

2.8. Effect of rotation

The effect of rotation through the Coriolis force is determined by the Coriolis number,

$$\mathrm{Co} = 2\Omega/u_{\rm rms}k_{\rm f} = 6\Omega\eta_{\rm t}/u_{\rm rms}^2, \tag{29}$$

where Ω is the angular velocity. Losada et al. (2012, 2013) found that NEMPI begins to be suppressed when $\mathrm{Co} \gtrsim 0.03$, which is a surprisingly small value. They only considered the case of a horizontal magnetic field. In the present case of a vertical magnetic field, we can use the axisymmetric model to include a vertical rotation vector $\boldsymbol{\Omega} = (0, 0, \Omega)$. We add the Coriolis force to the right-hand side of Eq. (2), i.e.,

$$\overline{\rho}\frac{\mathrm{D}\overline{\boldsymbol{U}}}{\mathrm{D}t} = \ldots - 2\boldsymbol{\Omega}\times\overline{\rho}\overline{\boldsymbol{U}}. \tag{30}$$

When adding weak rotation ($\mathrm{Co} = 0.01$) in Run Bv01/33, it turns out that magnetic flux concentrations develop on the periphery of the domain, similar to the case considered in Fig. 8. We have therefore reduced the radial extent of the domain to $r/H_\rho \le \pi/2$. The results are shown in Fig. 12.

In agreement with earlier studies, we find that rather weak rotation suppresses NEMPI. The magnetic structures become fatter and occur slightly higher up in the domain. For $\mathrm{Co} = 0.01$, the magnetic flux concentrations have become rather weak. If we write Co in terms of correlation of turnover time τ as $2\Omega\tau$, we find that the solar values of $\Omega = 3\times10^{-6}\,\mathrm{s}^{-1}$ corresponds to 30 min. According to stellar mixing length theory, this, in turn, corresponds to a depth of less than 2 Mm.

3. DNS and ILES studies

In the MFS discussed above, we have ignored the possibility of other terms in the parameterization of the mean-field Lorentz force. While this seems to capture the essence of earlier DNS (Brandenburg et al. 2013), this parameterization might not be accurate or sufficient in all respects. It is therefore useful to perform DNS to see how the results depend on scale separation, gravitational stratification, and Mach number.

3.1. DNS and ILES models

We have performed direct numerical simulations using both the Pencil Code[2] and Nirvana[3]. Both codes are fully compressible and are here used with an isothermal equation of state with $p = \rho c_{\rm s}^2$, where $c_{\rm s} = \mathrm{const}$ is the sound speed. The background stratification is then also isothermal. Turbulence is driven using volume forcing given by a function $\boldsymbol{f}$ that is δ-correlated in time and monochromatic in space. It consists of random non-polarized waves whose direction and phase change randomly at each time step.

In DNS we solve the equations for the velocity $\boldsymbol{U}$, the magnetic vector potential $\boldsymbol{A}$, and the density ρ,

$$\frac{\mathrm{D}\boldsymbol{U}}{\mathrm{D}t} = -c_{\rm s}^2\boldsymbol{\nabla}\ln\rho + \frac{1}{\rho}\boldsymbol{J}\times\boldsymbol{B} + \boldsymbol{f} + \boldsymbol{g} + \boldsymbol{F}_\nu, \tag{31}$$

$$\frac{\partial\boldsymbol{A}}{\partial t} = \boldsymbol{U}\times\boldsymbol{B} + \eta\nabla^2\boldsymbol{A}, \tag{32}$$

$$\frac{\partial\rho}{\partial t} = -\boldsymbol{\nabla}\cdot\rho\boldsymbol{U}, \tag{33}$$

where $\mathrm{D}/\mathrm{D}t = \partial/\partial t + \boldsymbol{U}\cdot\boldsymbol{\nabla}$ is the advective derivative, η is the magnetic diffusivity due to Spitzer conductivity of the plasma, $\boldsymbol{B} = \boldsymbol{B}_0 + \boldsymbol{\nabla}\times\boldsymbol{A}$ is the magnetic field, $\boldsymbol{B}_0 = (0, 0, B_0)$ is the imposed uniform vertical field, $\boldsymbol{J} = \boldsymbol{\nabla}\times\boldsymbol{B}/\mu_0$ is the current density, μ_0 is the vacuum permeability, $\boldsymbol{F}_\nu = \boldsymbol{\nabla}\cdot(2\nu\rho\mathbf{S})$ is the viscous force. The turbulent rms velocity is approximately independent of z. Boundary conditions are periodic in the horizontal directions (so vertical magnetic flux is conserved), and stress free on the upper and lower boundaries, where the magnetic field is assumed to be vertical, i.e., $B_x = B_y = 0$. In the ILES we solve the induction equation directly for $\boldsymbol{B}$, ignore the effects of explicit viscosity and magnetic diffusivity and use an approximate Riemann solver to keep the code stable and to dissipate kinetic and magnetic energies at small scales.

The simulations are characterized by specifying a forcing amplitude, which results in a certain rms velocity, $u_{\rm rms}$, and hence in a certain Mach number. Furthermore, the values of ν and η are quantified through the fluid and magnetic Reynolds numbers, $\mathrm{Re} = u_{\rm rms}/\nu k_{\rm f}$ and $\mathrm{Re}_M = u_{\rm rms}/\eta k_{\rm f}$, respectively. Their ratio is the magnetic Prandtl number, $\mathrm{Pr}_M = \nu/\eta$. Occasionally, we also quote $\tilde{\nu} = \nu/c_{\rm s}H_\rho$ and $\tilde{\eta} = \eta/c_{\rm s}H_\rho$.

An important diagnostics is the vertical magnetic field, B_z, at some horizontal layer. In particular, we use here the Fourier-filtered field, $\overline{B}_z$, which is obtained by removing all components with wavenumbers larger than 1/6 of the forcing wavenumber $k_{\rm f}$. This corresponds to a position in the magnetic energy spectrum where there is a local minimum, so we have some degree of scale separation between the forcing scale and the scale of the spot. We return to this in Sect. 3.5. To identify the magnetic field in the flux tube, we take the maximum of $\overline{B}_z$, either at each height

[2] http://pencil-code.googlecode.com
[3] http://nirvana-code.aip.de/

Table 2. Summary of DNS at varying $\tilde{B}_0$, and fixed values of $\tilde{\eta} = 2\times10^{-4}$, $\mathrm{Pr}_M = 0.5$, $\mathrm{Re} \approx 38$, $\mathrm{Ma} \approx 0.1$, $\hat{g} = 1$, $\hat{k}_\mathrm{f} = 30$, $\tau_\mathrm{td}/\tau_\mathrm{to} \approx 2700$, using 256^3 mesh points.

Run	$\hat{B}_0$	Re	Re_M	Ma	$\hat{B}_z$	$\hat{\overline{B}}_z$	$\tilde{R}$	$\tilde{z}_B^\mathrm{NL}$
(a)	0.0005	39	19	0.12	1.81	0.36	0.13	3.1
(b)	0.0010	39	19	0.12	2.68	1.00	0.11	1.8
(c)	0.0020	38	19	0.11	2.45	0.87	0.17	1.4
(d)	0.0050	37	18	0.11	3.47	1.25	0.22	−0.5
(e)	0.0100	35	18	0.11	3.95	1.49	0.29	−1.2
(f)	0.0200	31	16	0.09	4.21	1.26	0.45	$-\pi$

Notes. In all cases the number of resulting spots is unity. The positions $\tilde{z}_B^\mathrm{NL}$ agree with those marked in Fig. 13.

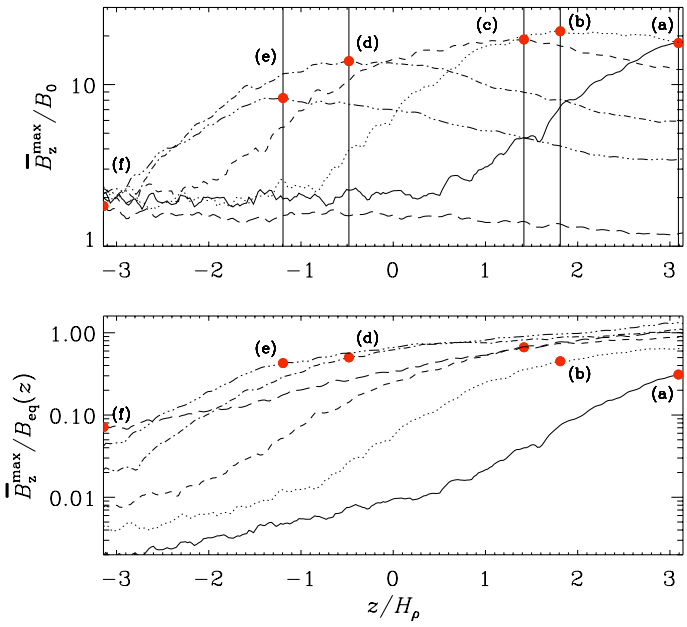

Fig. 13. Normalized vertical magnetic field profiles from DNS, $\overline{B}_z^\mathrm{max}/B_0$ (*top*) and $\overline{B}_z^\mathrm{max}/B_\mathrm{eq}(z)$ (*bottom*) for the six values of $B_0/B_{\mathrm{eq}0}$ listed in Table 2. In both panels, the red dots mark the maxima of $\overline{B}_z^\mathrm{max}/B_0$ at positions $\tilde{z}_B^\mathrm{NL}$. The labels (a)–(f) correspond to those in Table 2.

at one time, which is referred to as $\overline{B}_z^\mathrm{max}(z)$, or in the top layer at different times. The latter is used to determine the growth rate of the instability.

When comparing results for different values of g, it is convenient to keep the typical density at the surface the same. Since our hydrostatic stratification is given by Eq. (14), this is best done by letting the domain terminate at $z = 0$ and to consider the range $-L_z \le z \le 0$. In most of the cases we consider $L_z = \pi/k_1$, although this might in hindsight be a bit short in some cases. For comparison with earlier work of Brandenburg et al. (2013), we also present models in a domain $-\pi \le k_1 z \le \pi$.

3.2. Magnetic field dependence

In Table 2 and Fig. 13 we compare results for six values of $\tilde{B}_0 = B_0/(\mu_0\rho_0 c_{\mathrm{s}0}^2)^{1/2}$. These models are the same as those discussed in Brandenburg et al. (2013), where visualizations are shown for all six cases. Increasing $\tilde{B}_0$ leads to a decrease in the Mach number Ma and hence to a mild decline of Re and Re_M for $\tilde{B}_0 > 0.01$, corresponding to $B_0/B_{\mathrm{eq}0} > 0.1$. There is a slight increase of $\tilde{B}_z^\mathrm{max}$, while $\tilde{\overline{B}}_z^\mathrm{max}$ remains on the order of unity. This

Table 3. Summary of DNS at varying Pr_M, and fixed values of $\tilde{\eta} = 2\times10^{-4}$, $\tilde{B}_0 = 0.002$, $\mathrm{Re}_M \approx 20$–40, $\mathrm{Ma} \approx 0.1$, $\hat{g} = 1$, $\hat{k}_\mathrm{f} = 30$, $\tau_\mathrm{td}/\tau_\mathrm{to} \approx 2700$, using 256^3 mesh points.

$\tilde{\nu}$	Pr_M	Re_M	Ma	$\hat{\lambda}$	$\hat{B}_z$	$\hat{\overline{B}}_z$	$\tilde{R}$
4×10^{-5}	0.2	20	0.12	5.18	1.87	0.19	0.36
1×10^{-4}	0.5	19	0.11	1.33	2.45	0.87	0.17
2×10^{-4}	1	17	0.10	1.66	2.76	0.84	0.17
4×10^{-4}	2	14	0.08	1.46	2.78	0.64	0.20
5×10^{-4}	5	25	0.07	0.10	2.66	0.22	0.34
1×10^{-3}	10	19	0.06	0.04	2.87	0.28	0.30
5×10^{-4}	10	45	0.07	0.04	2.96	0.22	0.34

Notes. In all cases the number of spots is unity.

Table 4. Summary of DNS at varying Re and Re_M, and fixed values of $\tilde{\nu} = 10^{-4}$, $\tilde{B}_0 = 0.002$, $\mathrm{Pr}_M = 0.5$, $k_1 H_\rho = 1$, and $k_\mathrm{f} H_\rho = 30$.

Run	Re	Re_M	Ma	$\hat{B}_z$	$\hat{\overline{B}}_z$	$\tilde{R}$	Resol.
A30/1	38	19	0.11	2.45	0.87	0.17	256^3
B30/1	80	40	0.12	3.30	1.02	0.16	512^3
b30/1	200	40	0.12	3.45	1.10	0.15	512^3
C30/1	190	95	0.11	3.47	0.71	0.19	1024^3
D30/1	190	95	0.11	3.54	0.69	0.19	$1024^2\times1536$
E30/1	190	190	0.11	3.23	0.39	0.25	$1024^2\times1536$

is the case even for the largest value, $\tilde{B}_0 = 0.02$, when NEMPI is completely suppressed and there is no distinct maximum of $\overline{B}_z^\mathrm{max}/B_0$ in the upper panel of Fig. 13. This is why the visualization in Brandenburg et al. (2013) was featureless for $\tilde{B}_0 = 0.02$, even though $\tilde{B}_z/B_\mathrm{eq}(z) \approx 1$ at $z = z_\mathrm{top}$. Moreover, while $\tilde{B}_z^\mathrm{max}$ shows only a slight increase, the non-dimensional radius of the spot increases from 0.1 to about 0.4 as $\tilde{B}_0$ is increased.

3.3. Magnetic Prandtl number dependence

The results for different values of Pr_M are summarized in Table 3. It turns out that for $\mathrm{Pr}_M \ge 5$, no magnetic flux concentrations are produced. We recall that analysis based on the quasi-linear approach (which is valid for small fluid and magnetic Reynolds numbers) has shown that for $\mathrm{Pr}_M \ge 8$ and $\mathrm{Re}_M \ll 1$, no negative effective magnetic pressure is possible (Rüdiger et al. 2012; Brandenburg et al. 2012). Because of this, most of the earlier work used $\mathrm{Pr}_M = 0.5$ so as to stay below unity in the hope that this would be a good compromise between Pr_M being small and Re_M still being reasonably large. In fact, it now turns out that the difference in $\overline{B}_z^\mathrm{max}$ for $\mathrm{Pr}_M = 1$ and 1/2 be negligible, and even for $\mathrm{Pr}_M = 2$ the decline in $\overline{B}_z^\mathrm{max}$ is still small. For $\mathrm{Pr}_M = 0.2$, on the other hand, we find a large value of $\hat{\lambda}$, but a low saturation level. Again, this might be explained by the fact that the domain is not deep enough in the z direction, which can suppress NEMPI. Alternatively, the resolution of 256^3 might not be sufficient to resolve the longer inertial range for smaller magnetic Prandtl numbers. In Sect. 3.4 we present another case with $\mathrm{Pr}_M = 0.2$ where both the resolution and the Reynolds numbers are doubled, and $\overline{B}_z^\mathrm{max}$ is again large.

3.4. Reynolds number dependence

Increasing Re_M from 19 to 95, we see some changes; see Table 4. There is first a small increase of $\overline{B}_z^\mathrm{max}/B_\mathrm{eq}(z)$ from 0.87 to 1.02 as Re_M is increased from 19 to 40 (Run B30/1). Increasing Re

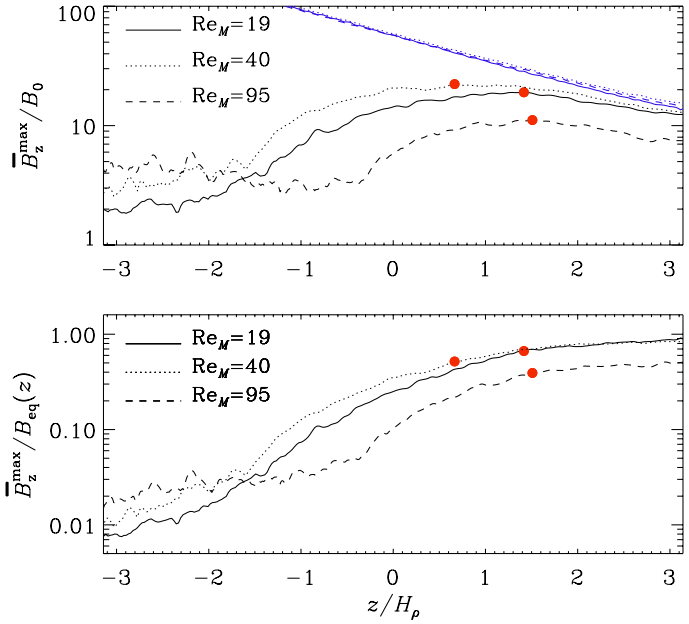

Fig. 14. Similar to Fig. 13, but for DNS Runs A30/1–C30/1 listed in Table 4, i.e., $\tilde{\nu} = 10^{-4}$, $\tilde{B}_0 = 0.002$, $\mathrm{Pr}_M = 0.5$, $k_1 H_\rho = 1$, and $k_{\rm f} H_\rho = 30$. In the *upper panel*, the blue lines denote $B_{\rm eq}(z)/B_0$ and in both panels, the red dots mark the maxima of $\overline{B}_z^{\max}/B_0$ at positions $\tilde{z}_B^{\rm NL}$.

to 200, but keeping $\mathrm{Re}_M = 40$, results in a further increase of $\overline{B}_z^{\max}/B_{\rm eq}(z)$ to 1.10 (Run b30/1). This is also an example of a strong flux concentration with $\mathrm{Pr}_M = 0.2$; cf. Sect. 3.3. However, when Re_M is increased further to 95, $\overline{B}_z^{\max}/B_{\rm eq}(z)$ decreases to about 0.71; see Table 4. Again, the weakening of the spot might be a consequence of the domain not being deep enough. Alternatively, it could be related to the occurrence of small-scale dynamo action, which is indicated by the fact that in deeper layers the small-scale magnetic field is enhanced in the run with the largest value of Re_M; see Fig. 14. In Run C30/1 with the largest value of Re_M, the spot is larger and more fragmented, but it still remains in place and statistically steady; see Fig. 15 and online material[4] for corresponding animations.

To eliminate the possibility of the domain not being deep enough, we have performed additional simulations where we have extended the domain in the negative z direction down to $z_{\rm bot}/H_\rho = -1.5\pi$. In Fig. 16 we show a computation of the resulting profiles of $\overline{B}_z^{\max}/B_0$ and $\overline{B}_z^{\max}/B_{\rm eq}(z)$. We also include here a run with $\mathrm{Pr}_M = 1$ instead of 0.5 (Run E30/1). It turns out that the strength of the spot is unaffected by the position of $z_{\rm bot}$ and that there is a deep layer below $z/H_\rho \approx -2$ in which there is significant magnetic field generation owing to small-scale dynamo action, preventing thereby also the value of $\overline{B}_z^{\max}/B_{\rm eq}(z)$ to drop below the desired value of 0.01. This might explain the weakening of the spot. This is consistent with earlier analytical (Rogachevskii & Kleeorin 2007) and numerical (Brandenburg et al. 2012) work showing a finite drop of the important NEMPI parameter $\beta_\star$ around $\mathrm{Re}_M = 60$.

3.5. Dependence on scale separation and stratification

We have performed various sets of additional simulations where we change $\hat{g}$ and/or $\hat{k}_{\rm f}$; see Table 5 and Fig. 17. In those cases, the vertical extent of the domain is from $-\pi$ to 0. As discussed in Sect. 3.1 this might be too small in some cases for NEMPI to develop fully. Nevertheless, in all cases there are clear indications for the occurrence of flux concentrations. The results regarding the growth rate of NEMPI are not fully conclusive, because the changes in $k_{\rm f}$ and H_ρ also affect turbulent-diffusive and turnover time scales. As shown in the appendix of Kemel et al. (2013) the normalized growth rate of NEMPI is given by:

$$\hat{\lambda} + 1 = 3\beta_\star\,(k_{\rm f}H_\rho)/(k_\perp H_\rho)^2, \tag{34}$$

which is not changed significantly for a vertical magnetic field; see Sect. 2.1. If $k_\perp H_\rho = \text{const.} \approx 0.7$, as suggested by the MFS of Sect. 2.4, we would expect $\hat{\lambda} + 1$ to be proportional to $k_{\rm f}H_\rho$, which is not in good agreement with the simulation results.

To shed some light on this, we now discuss horizontal power spectra of $B_z(x, y)$ taken at the top of the domain. These spectra are referred to as $E_{\rm M}^z(k)$ and are normalized by $B_{\rm eq}^2/k_{\rm f}$. In Run a30/4 with $\hat{g} = 4$ and $\hat{k}_{\rm f} = 30$, we have access to wavenumbers down to $k_1 H_\rho = 0.25$. The results in Fig. 18 show that there is significant power below $k_\perp H_\rho = 0.7$. This is in agreement with the MFS in the nonlinear regime; see Fig. 3. The time evolution of $E_{\rm M}^z(k)$ suggest a behavior similar to that of an inverse magnetic helicity cascade that was originally predicted by (Frisch et al. 1975) and later verified both in closure calculations (Pouquet et al. 1976) and DNS (Brandenburg 2001). Similar results with inverse spectral transfer are shown in Fig. 19 for DNS Run A40/1. The only difference between Runs A40/1 and a40/1 is the vertical extent of the domain, which is twice as tall in the former case ($3\pi H_\rho$ instead of $1.5\pi H_\rho$). We note in this connection that the spectra tend to show a local minimum near $k_{\rm f}/6$. This justifies our earlier assumption of separating mean and fluctuating fields at the wavenumber $k_{\rm f}/6$; see Sect. 3.1. The spectra also show something like an inertial subrange proportional to $k^{-5/3}$ (Fig. 19) or $k^{-2.5}$ (Fig. 18). The latter is close to the k^{-3} subrange in the MFS of Fig. 3. Those steeper spectra could be a symptom of a low Reynolds number or, alternatively, a consequence of most of the energy inversely "cascading" to larger scales in the latter two cases.

We have also checked how different kinds of helicities vary during NEMPI. In the present case, magnetic and kinetic helicities are fluctuating around zero, but cross helicity is not. The latter is an ideal invariant of the magnetohydrodynamic (MHD) equations, but in the present case of a stratified layer with a vertical net magnetic field, $\langle \boldsymbol{u} \cdot \boldsymbol{b} \rangle$ can actually be produced; see Rüdiger et al. (2011), who showed that

$$\langle \boldsymbol{u} \cdot \boldsymbol{b} \rangle \approx \eta_{\rm t} \boldsymbol{g} \cdot \boldsymbol{B}_0 / c_{\rm s}^2 = -\eta_{\rm t} B_0 / H_\rho. \tag{35}$$

In a particular case of Run 30/1, we find a time-averaged value of $\langle \boldsymbol{u} \cdot \boldsymbol{b} \rangle$ that would suggest that $\eta_{\rm t}/\eta_{\rm t0}$ is around 6, which is significantly larger than unity. This would agree with independent

Table 5. Summary of DNS at varying $\hat{k}_{\rm f} = k_{\rm f}/k_1$, $\tilde{k}_{\rm f} = k_{\rm f}H_\rho$, $\hat{g} = g/c_{\rm s}^2 k_1$, and fixed values of $\tilde{B}_0 = 0.02$, $\tilde{\eta}_0 = 2 \times 10^{-4}$, using resolutions of 256^3 mesh points (for Run a30/1), 512^3 mesh points (for Run a30/4, a10/3, and a30/3), as well as $1024^2 \times 384$ mesh points (for Runs a40/1 and A40/1).

Run	Pr_M	Re_M	Ma	$\hat{k}_{\rm f}$	$\tilde{k}_{\rm f}$	$\hat{g}$	$\hat{\lambda}$	$\hat{B}_z$	$\hat{\overline{B}}_z$
a30/1	1.0	16	0.09	30	30	1	0.94	3.09	0.78
a30/4	1.0	21	0.13	30	7.5	4	0.18	4.42	0.88
a10/3	1.0	63	0.13	10	3.4	3	–	4.83	0.40
a40/1	1.0	33	0.07	40	10	1	0.83	3.83	0.87
A40/1	1.0	33	0.07	40	10	1	1.05	5.81	1.41
a30/3	0.5	23	0.14	30	10	3	0.46	4.47	1.31

[4] http://www.nordita.org/~brandenb/movies/NEMPI/

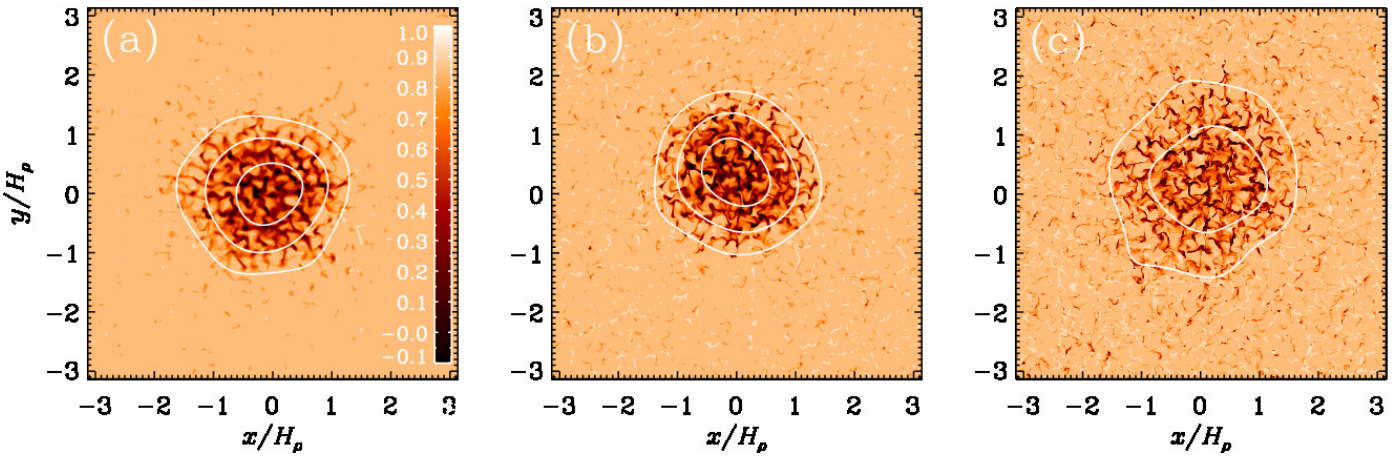

Fig. 15. Magnetic field configuration at the upper surface for DNS Runs A30/1–C30/1 at three values of the magnetic Reynolds number. The white contours represent the Fourier-filtered with $k_\perp \le k_f/6$; their levels correspond to $\overline{B}_z^{\max}/B_{\rm eq}(z_{\rm top}) = 0.05$, 0.2, and 0.4.

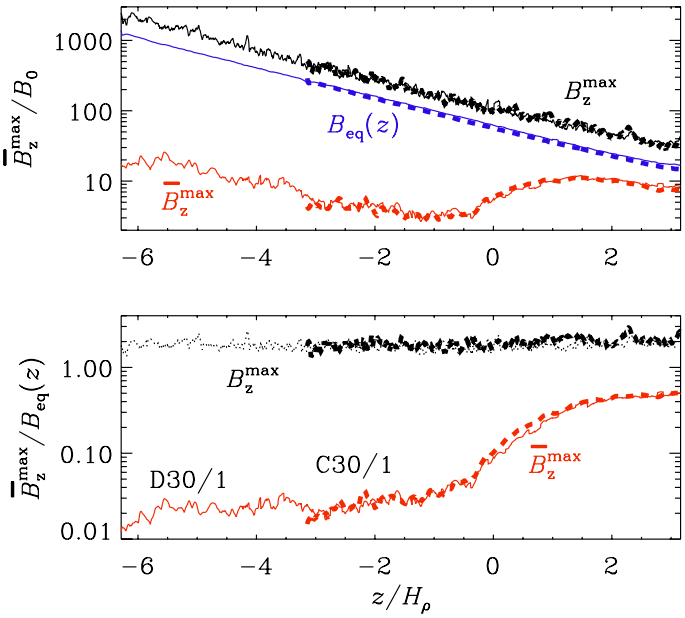

Fig. 16. Similar to Fig. 14, but for DNS Runs C30/1 ($z_{\rm bot}/H_\rho = -\pi$; thicker lines) and D30/1 ($z_{\rm bot}/H_\rho = -1.5\pi$; thinner lines) listed in Table 4, i.e., $\tilde{\nu} = 10^{-4}$, $\tilde{B}_0 = 0.002$, ${\rm Pr}_M = 0.5$, $k_1 H_\rho = 1$, and $k_f H_\rho = 30$. In the *upper panel*, the blue lines denote $B_{\rm eq}(z)/B_0$.

arguments in favor of having underestimated η_t; see the discussion in Sect. 2.5. In other words, if η_t were really larger than what is estimated based on the actual rms velocity, it would also explain why the diameter of tubes is bigger in the DNS than in the MFS.

3.6. Mach number dependence

To study the dependence on Mach number, it is useful to consider ILES without any explicit viscosity or magnetic diffusivity. In Figs. 20–22 we show the results for three values of Ma at $\hat{g} = gk_1/c_s^2 = 3$ and $\hat{k}_f = k_f/k_1$ using a resolution of $256^2 \times 128$ nodes on the mesh. In Table 6 we give a summary of various output parameters and compare with corresponding DNS. Note first of all that the results from ILES are generally in good agreement with the DNS. This demonstrates that the mechanism causing magnetic flux concentrations by NEMPI is robust

Table 6. Summary of DNS and ILES at varying values of Ma, all for $\hat{g} = 3$, $\hat{k}_f = 30$.

Run	$\tilde{B}_0$	${\rm Re}_M$	Ma	$\hat{\lambda}$	$\hat{B}_z$	$\hat{\overline{B}}_z$
D01	0.01	24	0.15	0.28	3.06	0.78
D02	0.02	24	0.14	0.46	4.47	1.31
D10	0.10	8	0.50	0.25	4.91	1.61
I03	0.10	–	0.16	>1	2.86	1.14
I10	0.10	–	0.34	>1	2.70	1.00
I30	0.10	–	0.68	>1	2.41	1.02

Notes. For ILES, no accurate values of $\hat{\lambda}$ are available. In the DNS, the resolution is 256^2 for Runs D01 and D02, and 512^2 for Run D10, while for Runs I03–I30 it is $256^2 \times 128$.

and not sensitive to details of the magnetic Reynolds number, provided that ${\rm Re}_M \gtrsim 10$. The normalized growth rate is in all three cases above unity.

As the Mach number is increased, the magnetic structures become smaller; seen in the left-hand panels of Fig. 22. Since the properties of NEMPI depend critically on the ratio $\overline{B}_z/B_{\rm eq}$, and since $B_{\rm eq}(z)$ and hence $B_{\rm eq0}$ increase with increasing Mach number, the decrease in the size of magnetic structures might just reflect the fact that for smaller values of $\overline{B}_z/B_{\rm eq0}$, NEMPI would operate at higher layers which are no longer included in our computational domain. Looking at Fig. 20, it is clear that the maximum of $\overline{B}_z/B_0$ moves to higher layers, but it is still well confined within the computational domain. Nevertheless, if one compensates for the decrease of $B_{\rm eq}$ by applying successively weaker mean fields when going to lower Mach number (right-hand panels of Fig. 22), the size of the emerging structures remains approximately similar and the curves of $\overline{B}_z/B_{\rm eq}$ lie now nearly on top of each other. This shows clearly that in our simulations with Ma ≈ 0.7, flux concentrations are well possible. This is important, because it allows for the possibility that the energy density of magnetic flux concentrations can become comparable with the thermal energy.

4. Possible application to sunspot formation

Compared with earlier studies of NEMPI using a horizontal imposed magnetic field, the prospects of applying it to the Sun

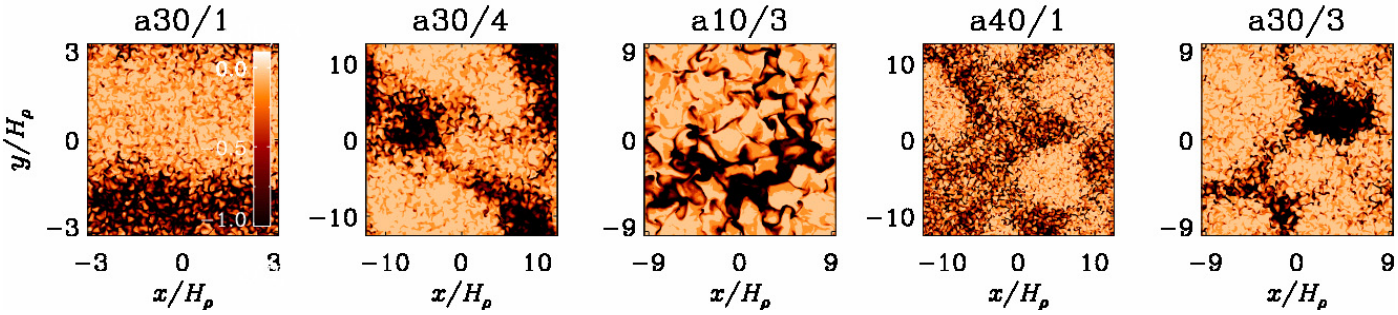

Fig. 17. Magnetic field configuration at the upper surface for DNS Runs a30/1–a30/3 of Table 5.

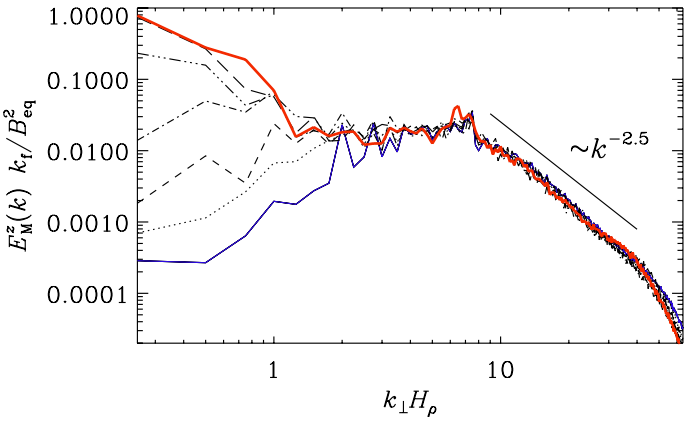

Fig. 18. Normalized spectra of B_z from DNS Run a30/4 at normalized times $t\eta_{t0}/H_\rho^2 \approx 0.2$, 0.5, 1, 2, 5, 10, and 20, for $\hat{g} \equiv g/c_s^2 k_f = 4$.

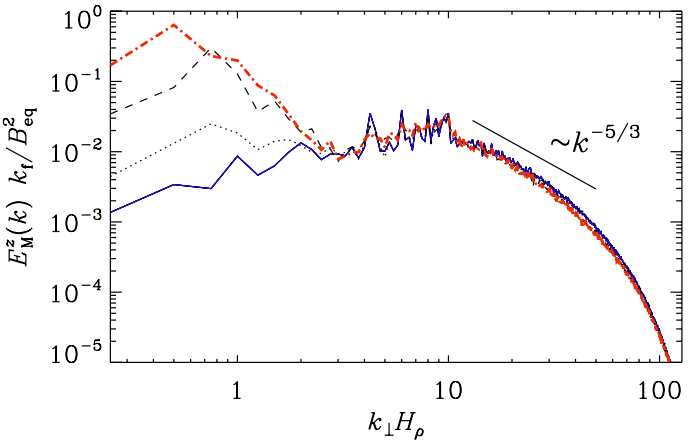

Fig. 19. Normalized spectra of B_z from DNS Run A40/1 at normalized times $t\eta_{t0}/H_\rho^2 \approx 0.2$, 0.5, 1, and 2.7 with $k_f H_\rho = 10$ and $k_1 H_\rho = 0.25$.

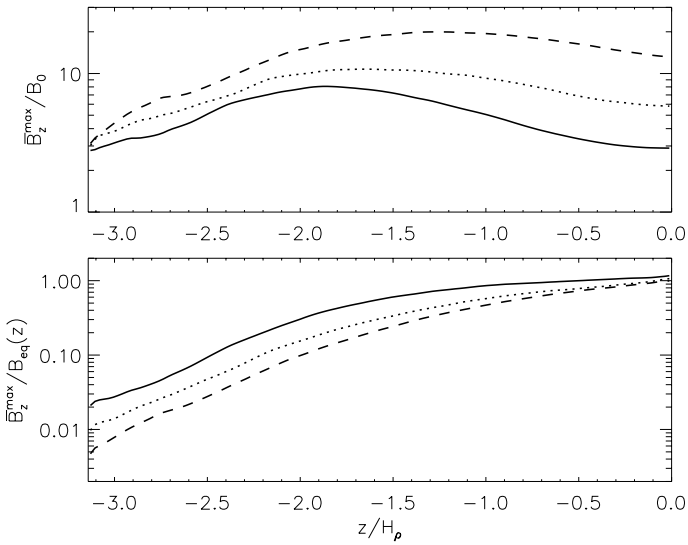

Fig. 20. Same as Fig. 13, but for the ILES runs with varying forcing amplitude. Note the different vertical extent of this set of models. The different lines indicate Ma = 0.16 (solid), 0.34 (dotted), and 0.68 (dashed).

have improved in the sense that the flux concentrations are now stronger when there is a vertical magnetic field. In particular, the resulting magnetic structures survive in the presence of larger Mach numbers up to 0.7, which is relevant to the photospheric layers of the Sun (Stein & Nordlund 1998). However, those structures do become somewhat weaker as the magnetic Reynolds number is increased sufficiently to allow for the presence of small-scale dynamo action. This was expected based on a certain drop of $\beta_\star$ for $\mathrm{Re}_M \gtrsim 60$ found in earlier simulations (Brandenburg et al. 2012), but the possibility of spot formation still persists. More specifically, we have seen that the largest field strength, $\overline{B}_z/B_0$, occurs at a height where $\overline{B}_z^{max}/B_{eq}$ is at least 0.4; see Fig. 16.

To speculate further regarding the applicability to sunspot formation, we must look at the mean-field models presented in Sect. 2. In particular, we have seen that spot formation occurs at a depth z_B^{NL} where $\overline{B}_z^{max}/B_{eq}$ is between 0.6 (for $\mathrm{Re}_M = 40$) and 0.4 (for $\mathrm{Re}_M = 95$); see Fig. 14 and Table 4. Larger ratios of $\overline{B}_z^{max}/B_{eq}$ occur in the upper layers, but then the absolute field strength is lower. In the MFS of Sect. 2, the value of $\overline{B}_z^{max}/B_{eq}$ at $z = z_B^{NL}$ is somewhat smaller (around 0.3), suggesting that the adopted set of mean-field parameters in Eq. (21) was slightly suboptimal. Nevertheless, those models show that the depth where NEMPI occurs and where the effective magnetic pressure is most negative is even further down, e.g., at $z/H_\rho \approx -7$; see Fig. 5. Furthermore, at the depth where $(-\mathrm{d}\mathcal{P}_{\rm eff}/\mathrm{d}\ln\beta^2)^{1/2}$ is maximum, i.e., where NEMPI is strongest according to theory, we find $\overline{B}_z^{max}/B_{eq} \approx 0.05$. Thus, there is an almost tenfold increase of the absolute field strength between the depth were NEMPI occurs and where the field is strongest.

As we have seen from Fig. 5, this increase is caused solely by hydraulic effects, similar to what Parker (1976, 1978) anticipated over 35 years ago. Our isothermal models clearly do demonstrate the hydraulic effect due to downward suction, but we cannot expect realistic estimates for the resulting field amplification. Parker (1978) gives more realistic estimates, but in his work the source of downward flows remained unclear. Our present work suggests that NEMPI might drive such motion, but in realistic simulations it would be harder to identify this

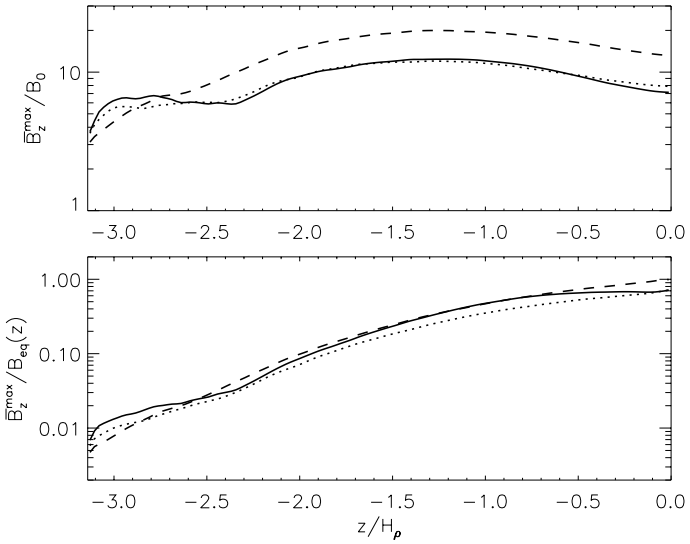

Fig. 21. Same as Fig. 20, but for the ILES runs which vary both the forcing amplitude and the imposed magnetic field at the same time, keeping the *relative* field strength comparable. The different lines again indicate Ma = 0.16 (solid), 0.35 (dotted), and 0.68 (dashed), and agree markedly well in the *lower panel* where we plot relative to $B_{\rm eq}(z)$.

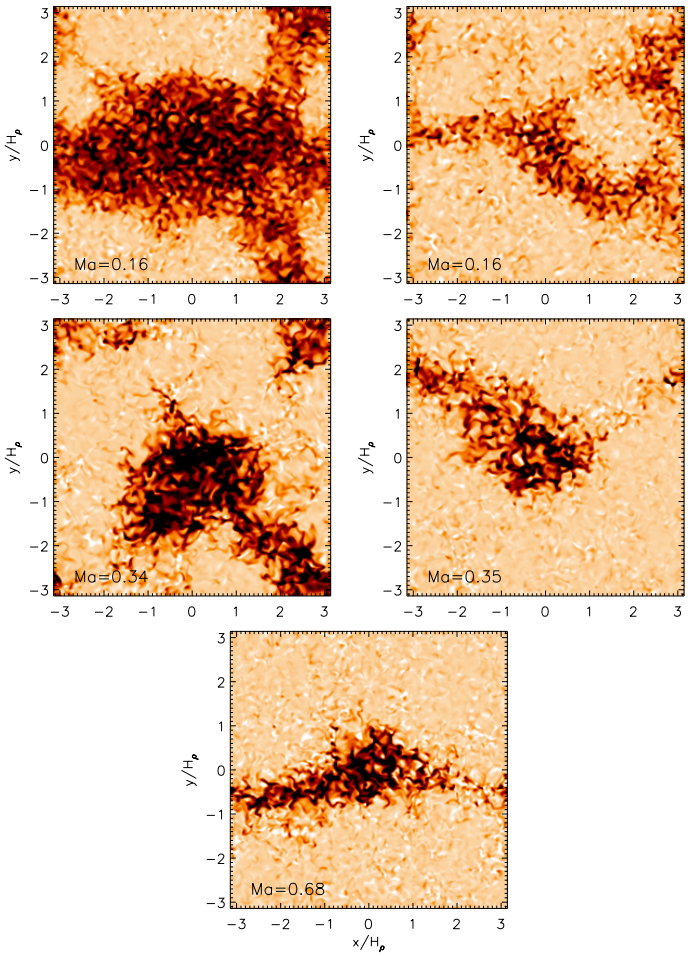

Fig. 22. Surface appearance of the vertical magnetic field, $B_z^{\rm max}$, in the ILES simulations with different Mach numbers (*top to bottom*). The color coding shows $B_z^{\rm max}/B_{\rm eq}$ in the range of −0.1 (white) to +1.0 (black). Root-mean-square Mach numbers are given by the labels. For the *upper two rows* with lower Mach number, the *left column* is for fixed initial mean field, whereas in the *right column* the initial field is adjusted between the runs, such that the field strength remains constant relative to the kinetic energy in the background turbulence.

as the sole mechanism. Another mechanism might simply be large-scale hydrodynamic convection flows that would continue deeper down to the lower part of the supergranulation layer at depths between 20 and 40 Mm. Some indications of this have now been seen in simulations of Stein & Nordlund (2012). Whether the reason for flux concentrations is then NEMPI or convection can only be determined through careful numerical experiments comparing full MHD with the case of a passive vector field. Such a field would still be advected by convective flows but would not contribute to the dynamical effects that would be required if NEMPI were to be responsible.

In addition to the magnetic field strength of flux concentrations, there might also be issues concerning their size. Usually they are not much larger than about 5 density scale heights; see, e.g., Fig. 15. This might be too small to explain sunspots. On the other hand, in the supergranulation layer, the density scale height increases, and larger scale structures might be produced at those depths.

To make this more concrete, let us discuss a possible scenario. At a depth of 3 Mm, the equipartition field strength is about 2 kG, and this might be where the sunspot field is strongest. If NEMPI was to be responsible for this, we should expect the effective magnetic pressure to be negative at a depth of about 10 Mm. Here, the equipartition field strength is about 3 kG. If NEMPI operates at $\overline{B}_z^{\rm max}/B_{\rm eq} \approx 0.1$, this would correspond to $\overline{B}_z^{\rm max} \approx 300$ G, which appears plausible. At that depth, the density scale height is also about 10 Mm. Thus, if magnetic flux concentrations have a size of 5 density scale heights, then this would correspond to 50 Mm at that depth. To produce spots higher up, the field would need to be more concentrated, which would reduce the size by a factor of 3 again. However, given the many uncertainties, it is impossible to draw any further conclusions until NEMPI has been studied under more realistic conditions relevant to the Sun.

5. Conclusions

Using DNS, ILES and MFS in a wide range of parameters we have demonstrated that an initially uniform vertical weak magnetic field in strongly stratified MHD turbulence with large scale separation results in the formation of circular magnetic spots of equipartition and super-equipartition field strengths. Although we have confirmed that the normalized horizontal wavenumber of magnetic flux concentrations is $k_\perp H_\rho \approx 0.8$, as found earlier for horizontal imposed field (Kemel et al. 2013), it is now clear that in the nonlinear regime smaller values can be attained. This happens in a fashion reminiscent of an inverse cascade or inverse transfer[5] in helically forced turbulence (Brandenburg 2001). In the present case, this inverse transfer is found both in MFS and in DNS. This property helps explaining the possibility of larger length scales separating different flux concentrations.

The study of axisymmetric MFS helps understanding the dependence of NEMPI on the parameters $\beta_\star$ and $\beta_{\rm p}$, which determine the parameterization of the effective magnetic

[5] In both cases, the transfer is *nonlocal* in wavenumber space. It is therefore more appropriate to use the term inverse transfer instead of inverse cascade.

pressure, $\mathcal{P}_{\rm eff}(\beta)$. It was always clear that changes in those parameters can significantly change the functional form of $\mathcal{P}_{\rm eff}(\beta)$, and yet the resulting growth rate of NEMPI was found to depend mainly on the value of $\beta_\star$. We now see, however, that the shape of the resulting solutions still depends on the value of $\beta_{\rm p}$, in addition to a dependence on $\beta_\star$. In fact, smaller values of $\beta_{\rm p}$ as well as larger values of $\beta_\star$ both result in longer structures. This is important background information in attempts to find flux concentrations in DNS, where the domain might not always be tall enough. As a rule of thumb, we can now say that the domain is deep enough if the resulting large-scale magnetic field is below 1% of the equipartition value. This is confirmed by Figs. 13 and 14 as well as Figs. 20 and 21, where all runs with $\overline{B}_z^{\rm max}/B_{\rm eq}(z) \le 0.01$ at $z = z_{\rm bot}$ reach $\overline{B}_z^{\rm max}/B_{\rm eq}(z) = O(1)$ at $z = z_{\rm top}$, provided the domain is also high enough. A limited extent at the top appears to be less critical than at the bottom, because NEMPI still develops in almost the same way as before.

It is important to emphasize that the formation of magnetic flux concentrations is equally well possible at large Mach numbers. This is important in view of applications to the Sun, where in the upper layers Ma ≈ 0.5 can be expected. Nevertheless, our present investigations have not yet been able to address the question whether sunspots can really form through NEMPI. For that, we would need to abandon the assumption of isothermality. Nevertheless, we expect the basic feature of downflows along flux tubes to persist also in that case. It is the associated inflow from the side that keeps the tube concentrated. Such flows have indeed been seen in local helioseismology (Zhao et al. 2010). Those authors also find an additional outflow higher in the photosphere that is known as the Evershed flow.

We expect that the downflow in the tube plays an important role in an unstably stratified layer, such as in the Sun, where it brings low entropy material to deeper layers, lowering therefore the effective temperature in the magnetic tubes. Future work should hopefully be able to demonstrate that in detail. The conceptual difference between NEMPI and other mechanisms may not always be very clear. However, by using an isothermal layer, we can be sure that convection is not operating. Thus, the phenomenon of flux segregation found by Tao et al. (1998) would not work. Conversely, however, NEMPI might well be a viable explanation for this phenomenon too. Whether the concept of flux expulsion can really serve as an alternative paradigm is unclear, because it is difficult to draw any quantitative predictions from it. In particular, flux expulsion does not make any reference to turbulent pressure or its suppression. Instead, the source of free energy is more directly potential energy which can be tapped through the superadiabatic gradient in convection. By contrast, the source of free energy for NEMPI is turbulent energy. The other possibility discussed above is the network of downdrafts associated with the supergranulation layer (Stein & Nordlund 2012). This mechanism is not easily disentangled from NEMPI, because both imply flux concentrations in downdrafts. However, in an isothermal layer, we can be sure that supergranulation flows are absent, so NEMPI is the only known mechanism able to explain the flux concentrations shown in the present paper.

Acknowledgements. This work was supported in part by the European Research Council under the AstroDyn Research Project No. 227952, by the Swedish Research Council under the project grants 2012-5797 and 621-2011-5076 (AB), by the European Research Council under the Atmospheric Research Project No. 227915, and by a grant from the Government of the Russian Federation under contract No. 11.G34.31.0048 (NK, IR). We acknowledge the allocation of computing resources provided by the Swedish National Allocations Committee at the Center for Parallel Computers at the Royal Institute of Technology in Stockholm and the National Supercomputer Centers in Linköping, the High Performance Computing Center North in Umeå, and the Nordic High Performance Computing Center in Reykjavik. Part of this work used the Nirvana code version 3.3, developed by Udo Ziegler at the Leibniz-Institut für Astrophysik Potsdam (AIP).

References

Biskamp, D. 1993, Nonlinear magnetohydrodynamics (Cambridge: Cambridge University Press)
Brandenburg, A. 2001, ApJ, 550, 824
Brandenburg, A. 2005, ApJ, 625, 539
Brandenburg, A., Kemel, K., Kleeorin, N., Mitra, D., & Rogachevskii, I. 2011, ApJ, 740, L50
Brandenburg, A., Kemel, K., Kleeorin, N., Rogachevskii, I. 2012, ApJ, 749, 179
Brandenburg, A., Kleeorin, N., & Rogachevskii, I. 2013, ApJ, 776, L23
Cheung, M. C. M., Rempel, M., Title, A. M., & Schüssler, M. 2010, ApJ, 720, 233
Fan, Y. 2009, Liv. Rev. Sol. Phys., 6, 4
Frisch, U., Pouquet, A., Léorat, J., & Mazure, A. 1975, J. Fluid Mech., 68, 769
Grinstein, F. F., Fureby, C., & DeVore, C. R. 2005, Int. J. Num. Meth. Fluids, 47, 1043
Kemel, K., Brandenburg, A., Kleeorin, N., Mitra, D., & Rogachevskii, I. 2012a, Sol. Phys., 280, 321
Kemel, K., Brandenburg, A., Kleeorin, N., & Rogachevskii, I. 2012b, Astron. Nachr., 333, 95
Kemel, K., Brandenburg, A., Kleeorin, N., Mitra, D., & Rogachevskii, I. 2013, Sol. Phys., 287, 293
Kitiashvili, I. N., Kosovichev, A. G., Wray, A. A., & Mansour, N. N. 2010, ApJ, 719, 307
Kleeorin, N., & Rogachevskii, I. 1994, Phys. Rev. E, 50, 2716
Kleeorin, N. I., Rogachevskii, I. V., & Ruzmaikin, A. A. 1989, Sov. Astron. Lett., 15, 274
Kleeorin, N. I., Rogachevskii, I. V., & Ruzmaikin, A. A. 1990, Sov. Phys. JETP, 70, 878
Kleeorin, N., Mond, M., & Rogachevskii, I. 1993, Phys. Fluids B, 5, 4128
Kleeorin, N., Mond, M., & Rogachevskii, I. 1996, A&A, 307, 293
Losada, I. R., Brandenburg, A., Kleeorin, N., Mitra, D., & Rogachevskii, I. 2012, A&A, 548, A49
Losada, I. R., Brandenburg, A., Kleeorin, N., & Rogachevskii, I. 2013, A&A, 556, A83
Parker, E. N. 1976, ApJ, 210, 816
Parker, E. N. 1978, ApJ, 221, 368
Pouquet, A., Frisch, U., & Léorat, J. 1976, J. Fluid Mech., 77, 321
Rempel, M. 2011, ApJ, 740, 15
Rogachevskii, I., & Kleeorin, N. 2007, Phys. Rev. E, 76, 056307
Rüdiger, G., Kitchatinov, L. L., & Brandenburg, A. 2011, Sol. Phys., 269, 3
Rüdiger, G., Kitchatinov, L. L.& Schultz, M. 2012, Astron. Nachr., 333, 84
Spruit, H. C. 1979, Sol. Phys., 61, 363
Spruit, H. C. 1981, A&A, 102, 129
Sur, S., Brandenburg, A., & Subramanian, K. 2008, MNRAS, 385, L15
Stein, R. F., & Nordlund, Å. 1998, ApJ, 499, 914
Stein, R. F., & Nordlund, Å. 2012, ApJ, 753, L13
Tao, L., Weiss, N. O., Brownjohn, D. P., & Proctor, M. R. E. 1998, ApJ, 496, L39
Warnecke, J., Losada, I. R., Brandenburg, A., Kleeorin, N., & Rogachevskii, I. 2013, ApJ, 777, L37
Zhao, J., Kosovichev, A. G., & Sekii, T. 2010, ApJ, 708, 304
Ziegler U., 2004, J. Comput. Phys., 196, 393